Imaging increased metabolism in the spinal cord in mice after middle cerebral artery occlusion

Ni, Ruiqing ; Straumann, Nadja ; Fazio, Serana ; Dean-Ben, Xose Luis ; Louloudis, Georgios ; Keller, Claudia ; Razansky, Daniel ; Ametamey, Simon ; Mu, Linjing ; Nombela-Arrieta, César ; Klohs, Jan

Abstract: Emerging evidence indicates crosstalk between the brain and hematopoietic system following cerebral ischemia. Here, we investigated metabolism and oxygenation in the spleen and spinal cord in a transient middle cerebral artery occlusion (tMCAO) model. Sham-operated and tMCAO mice underwent [^{18}F]fluorodeoxyglucose (FDG)-positron emission tomography (PET) to assess glucose metabolism. Naïve, sham-operated and tMCAO mice underwent multispectral optoacoustic tomography (MSOT) assisted by quantitative model-based reconstruction and unmixing algorithms for accurate mapping of oxygenation patterns in peripheral tissues at 24 h after reperfusion. We found increased [^{18}F]FDG uptake and reduced MSOT oxygen saturation, indicating hypoxia in the thoracic spinal cord of tMCAO mice compared with sham-operated mice but not in the spleen. Reduced spleen size was observed in tMCAO mice compared with sham-operated mice ex vivo. tMCAO led to an increase in the numbers of mature T cells in femoral bone marrow tissues, concomitant with a stark reduction in these cell subsets in the spleen and peripheral blood. The combination of quantitative PET and MSOT thus enabled observation of hypoxia and increased metabolic activity in the spinal cord of tMCAO mice at 24 h after occlusion compared to sham-operated mice.

DOI: https://doi.org/10.1016/j.pacs.2023.100532

Photoacoustics 32 (2023) 100532

Contents lists available at ScienceDirect

Photoacoustics

journal homepage: www.elsevier.com/locate/pacs

Imaging increased metabolism in the spinal cord in mice after middle cerebral artery occlusion

Ruiqing Ni [a,b,c,*], Nadja Straumann [a], Serana Fazio [d], Xose Luis Dean-Ben [b], Georgios Louloudis [b], Claudia Keller [e], Daniel Razansky [b,c], Simon Ametamey [e], Linjing Mu [e], César Nombela-Arrieta [d], Jan Klohs [b,**]

[a] Institute for Regenerative Medicine, University of Zurich, Zurich, Switzerland
[b] Institute for Biomedical Engineering, Department of Information Technology and Electrical Engineering, University of Zurich & ETH Zurich, Zurich, Switzerland
[c] Zentrum für Neurowissenschaften Zurich, Zurich, Switzerland
[d] Department of Medical Oncology and Hematology, University and University Hospital Zurich, Zurich, Switzerland
[e] Center for Radiopharmaceutical Sciences ETH, PSI and USZ, Institute of Pharmaceutical Sciences, Department of Chemistry and Applied Biosciences, ETH Zurich, Zurich, Switzerland

ARTICLE INFO

Keywords:
fluorodeoxyglucose (FDG)
Ischemic stroke
Metabolism
MSOT
Optoacoustic tomography
Oxygenation
Positron emission tomography
Spinal cord
Spleen

ABSTRACT

Emerging evidence indicates crosstalk between the brain and hematopoietic system following cerebral ischemia. Here, we investigated metabolism and oxygenation in the spleen and spinal cord in a transient middle cerebral artery occlusion (tMCAO) model. Sham-operated and tMCAO mice underwent [^{18}F]fluorodeoxyglucose (FDG)-positron emission tomography (PET) to assess glucose metabolism. Naïve, sham-operated and tMCAO mice underwent multispectral optoacoustic tomography (MSOT) assisted by quantitative model-based reconstruction and unmixing algorithms for accurate mapping of oxygenation patterns in peripheral tissues at 24 h after reperfusion. We found increased [^{18}F]FDG uptake and reduced MSOT oxygen saturation, indicating hypoxia in the thoracic spinal cord of tMCAO mice compared with sham-operated mice but not in the spleen. Reduced spleen size was observed in tMCAO mice compared with sham-operated mice *ex vivo*. tMCAO led to an increase in the numbers of mature T cells in femoral bone marrow tissues, concomitant with a stark reduction in these cell subsets in the spleen and peripheral blood. The combination of quantitative PET and MSOT thus enabled observation of hypoxia and increased metabolic activity in the spinal cord of tMCAO mice at 24 h after occlusion compared to sham-operated mice.

1. Introduction

Brain injury due to cerebral ischemia results in early activation of the immune system that is at a later stage followed by immunodepression. In experimental cerebral ischemia, the inflammatory response is crucially involved in secondarily enhancing lesion growth but is also indispensable for tissue repair and regeneration. Immunodepression after cerebral ischemia increases the susceptibility to infections [1], leading to impaired recovery and death. [2,3]. Emerging evidence indicates brain-periphery crosstalk and activation of the hematopoietic system after ischemic stroke via the sympathetic nervous system [4]. Thus, interactions between the brain and the immune system are very relevant to the overall outcome after cerebral ischemia [5], and understanding these processes is key before immunomodulatory therapy can be applied to stroke patients. Monocytes are mobilized from the spleen, which is the largest lymphatic organ in the body, upon injury [6]. The levels of circulating neutrophils and monocytes increase in the circulation after ischemic stroke in animal models [7,8]. These myeloid cells are recruited to the ischemic brain [9,10]. Altered splenic function, reductions in spleen weight and a decrease in monocytes/macrophages in the spleen have been demonstrated in both permanent and transient middle cerebral artery occlusion (pMCAO and tMCAO) models [11–15]. In addition, tMCAO induces rapid activation of the peripheral immune system in the spinal cord and bone marrow (BM), the primary site of hematopoiesis, as well as blood–spinal cord barrier alterations in rodent and primate models [12,16–20]. A previous study showed that tMCAO

* Corresponding author at: Institute for Regenerative Medicine, University of Zurich, Zurich, Switzerland.
** Corresponding author.
E-mail addresses: ruiqing.ni@uzh.ch (R. Ni), klohs@biomed.ee.ethz.ch (J. Klohs).

https://doi.org/10.1016/j.pacs.2023.100532
Received 12 August 2022; Received in revised form 13 July 2023; Accepted 13 July 2023
Available online 15 July 2023

activated BM hematopoietic stem cells (HSCs) and downstream hematopoietic progenitors, leading to an increased output of inflammatory monocytes and neutrophils [4].

Non-invasive monitoring of the activation of hematopoietic organs is an active area of research. Studies have shown that progenitor and immune cell function are controlled by tissue oxygen tension and glucose metabolism [21,22]. Few studies have noninvasively investigated metabolic processes in hematopoietic organs in experimental models of cerebral ischemia and stroke patients. [^{18}F]fluorodeoxyglucose (FDG) PET studies have been applied to assess glycolysis in hematopoietic organs in patients with a variety of disease conditions, including infection [23], cancer [24], vasculitis [25], and cardiovascular diseases [26,27]. Studies have found marked elevations in [^{18}F]FDG uptake in the spleen and spinal cord, which was associated with systemic inflammatory markers and future cardiovascular events. Studies have demonstrated decreased [^{18}F]FDG uptake in lumbar vertebrae (L4, L5), and no difference in the spleen of ischemic stroke patients compared to controls has been reported, but PET was performed at the chronic stage of the disease with a larger variability [28]. [^{18}F]FDG PET of hematopoietic organs in MCAO models, where the assessment of earlier time points after cerebral ischemia with lower temporal variability is easier to attain, has thus far not been performed. Another regulator of immune and stem cell function in hematopoietic organs is local tissue oxygen tension [22]. Optoacoustic imaging allows for the non-invasive assessment of blood oxygenation relatively deep in tissue (mm to cm range) [29–33]. Multi-spectral optoacoustic tomography (MSOT) has been previously employed to detect functional and molecular alterations in the brain of ischemic stroke animal models, including reduced oxygen saturation (sO_2) and increased inflammation [34–39], but not yet in the periphery.

We hypothesize that tMCAO affects tissue oxygenation and glucose metabolism in the peripheral immune system spleen, femur bone marrow and spinal cord in the tMCAO mouse model at an early phase (24 h after occlusion). In this study, we aimed to noninvasively image the metabolic alterations in the hematopoietic organs in response to tMCAO with [^{18}F]FDG PET and MSOT and evaluate immune and progenitor cell responses using flow cytometry.

2. Materials and methods

2.1. Animal model

Thirty-one male C57BL/6 J mice (Janvier, France) weighing 20–25 g and 8–10 weeks of age were used. Animals were housed in ventilated cages inside a temperature-controlled room under a 12 h dark/light cycle. Pelleted food (3437PXL15, CARGILL) and water were provided ad libitum. Paper tissue and red mouse house® (Tecniplast, Milan, Italy) shelters were placed in cages for environmental enrichment. All experiments were performed in accordance with the Swiss Federal Act on Animal Protection and were approved by the Cantonal Veterinary Office Zurich (permit number: ZH080/18). We confirm compliance with the NC3Rs ARRIVE 2.0 guidelines on reporting of *in vivo* experiments. Power analysis was performed to calculate the number of animals needed. Mice were randomly allocated to naïve (n = 8), sham (n = 13) or tMCAO (n = 10) groups. For MSOT, the exclusion criteria are the dark pigments in the trunk and limb, which influence the MSOT image quality. Thus, mice with strong dark pigmentation after shaving were included as the naïve group only for FACS analysis without imaging. Details on the numbers of animals that underwent experimental procedures are shown in STable 1.

2.2. Transient middle cerebral artery occlusion

Transient middle cerebral artery occlusion (tMCAO) was induced using the intraluminal filament technique [40,41]. The sham operation involved anaesthesia and analgesia and surgical procedures, but the filament was withdrawn immediately. The protocol involved 10 min for the insertion procedure, 60 min for passive insertion, and 5 min for removal. The total time for surgical procedures is 15 min (in addition to the passive filament insertion time). Anaesthesia was induced by using 3% isoflurane (Abbott, Cham, Switzerland) in a mixture of O_2 (200 ml/min) and air (800 ml/min) supplied via face mask. Anaesthesia was maintained with 1.5–2% isoflurane in a mixture of O_2 (200 ml/min) and air (800 ml/min), supplied via face mask. Before the surgical procedure, buprenorphine was administered subcutaneously (s.c.) injection (0.1 mg/kg; 1 ml Temgesic + 5 ml NaCl, 2 µl Temgesic/g of body weight). Temperature was controlled during the surgery and kept constant at 36.5 ± 0.5℃ with a feedback-controlled warming pad system. A midline neck incision was made, and the left common carotid artery was ligated proximal to the bifurcation of the internal carotid artery and external carotid artery. Subsequently, the left external carotid artery was isolated and ligated. A suture was placed around the internal carotid artery to temporarily restrict blood flow. A small incision was made in the common carotid artery, and an 11-mm long silicone-coated monofilament (171956PK5Re, Doccol Corporation, USA) was introduced and advanced until it occluded the middle cerebral artery. A suture around the internal carotid artery secured the filament in position. In tMCAO animals, the filament was left in place for 60 min, while in sham animals, the suture was withdrawn immediately, and the internal carotid artery was ligated. After occlusion of the vessel or sham, animals were transferred to a heated recovery box and allowed to wake up. After 60 min, all animals were anaesthetized. In tMCAO, the filament was withdrawn, and the internal carotid artery was ligated. The surgical incision was closed with a suture, and animals were placed in a heated recovery box for 2 h. A second dose of buprenorphine was administered s.c. injection (Temgesic, 0.1 mg/kg; 1 ml Temgesic + 5 ml NaCl, 2 µl Temgesic/g of body weight) 4 h after reperfusion and supplied thereafter by drinking water (0.1 mg/kg body weight) until the end of the study. Buprenorphine was then given twice s.c. every 6–8 h on the day of surgery and thereafter supplied by drinking water (1 mg/kg) for 36 h. Animals received softened chow in a weighing boat placed on the cage floor to encourage eating. tMCAO animals were excluded from the study if they met one of the following criteria: Bederson score of 0, no reflow after filament removal, and premature death.

2.3. [^{18}F]FDG-µPET/CT

Four sham-operated and four tMCAO mice underwent microPET imaging at 24 h after reperfusion. Scans were performed with a calibrated SuperArgus µPET/CT scanner (Sedecal, Spain) with an axial field-of-view of 4.8 cm and a spatial resolution of 1.6–1.7 mm (full width at half maximum). tMCAO and sham-operated C57BL/6 J mice were anaesthetized with isoflurane (2.5%) in oxygen/air (1:1) during tracer injection and the whole scan time period. The formulated radioligand solution ([^{18}F]FDG: 9.9–11 MBq) was administered via tail vein injection. Mice were dynamically scanned until 60 min after injection. Body temperature was monitored by a rectal probe and kept at 37 °C by a heated air stream (37 °C). The anaesthesia depth was measured by respiratory frequency (SA Instruments, Inc., USA). µPET acquisitions were combined with CT for anatomical orientation and attenuation correction. The obtained data were reconstructed in user-defined time frames with a voxel size of 0.3875 × 0.3875 × 0.775 mm^3 as previously described [42].

2.4. PET data analysis

Images were processed using PMOD 4.2 software (PMOD Technologies Ltd., Zurich, Switzerland). Spleen, cervical and thoracic spinal cord volumes of interest (VOIs) were defined based on the CT contrast. The time-activity curves were deduced from specific VOIs. Radioactivity is presented as the standardized uptake value (SUV) (decay-corrected radioactivity per cm^3 divided by the injected dose per gram body weight). The SUV signal was averaged from 18 to 53.5 min. Vertebral

VOIs were drawn manually similar to a previous report (Fig. 1) [43].

2.5. MSOT

Three naïve, six sham and four tMCAO mice underwent MOST imaging at 24 h after reperfusion. An MSOT inVision 128 imaging system (iThera Medical, Germany) was used as described previously [44–46]. Briefly, a tunable (680–980 nm) optical parametric oscillator pumped by a Nd:YAG laser provides < 10 ns excitation pulses at a frame rate of 10 Hz with a wavelength tuning speed of less than 10 ms and a peak pulse energy of 100 mJ at 730 nm. Ten arms, each containing an optical fibre bundle, provide even illumination of a ring-shaped light strip with a width of approx. 8 mm. For ultrasound detection, an array of 128 cylindrically focused ultrasound transducers with a center frequency of 5 MHz (60% bandwidth), organized in a concave array of 270 degree angular coverage and a curvature radius of 4 cm, were used.

For *in vivo* MSOT measurement, animals were anaesthetized with 4% isoflurane and maintained at 1.5% isoflurane in a 1:4 oxygen/air mixture supplied via a nose cone. Mice were depilated around the body parts of interest (approximately below the 5th rib) and placed in a mouse holder in the supine position with a cuff around the legs. Preheated ultrasound gel (Diagramma, Switzerland) was applied to the mouse body for ultrasonic coupling, and the animals were wrapped in a polyethylene membrane. The mouse holder was placed in an imaging chamber filled with water with the temperature controlled at 36.5 °C. Images were acquired at 5 wavelengths (715, 730, 760, 800, and 850 nm) for 135–140 consecutive slices with a step size of 0.3 mm and 10 averages. The total acquisition time was approximately 10 min.

2.6. MSOT image reconstruction and spectral unmixing

To avoid negative-value artifacts present in the images reconstructed with standard back-projection algorithms [26]. MSOT images were processed with a dedicated non-negative constrained model-based (NNMB) reconstruction-unmixing framework [47], which is also known to facilitate quantification of oxygenation values in the images [43]. Specifically, images corresponding to different excitation wavelengths were first reconstructed with an NNMB algorithm. Subsequently, linear unmixing was also performed with an NNMB algorithm considering the theoretical absorption spectra of deoxygenated (Hb) and oxygenated (HbO_2) hemoglobin. For comparison, the images were also processed with the data analysis system software (iTheraMedical, Germany). This consists of a standard model-based reconstruction algorithm followed by linear spectral unmixing but does not include non-negative constraints. Unmixed images represent the biodistribution of Hb and HbO_2. The sO_2 of the tissue (the capillaries/microvasculature composing the tissue) was then calculated as

$$sO2 = \frac{HbO2}{Hb + HbO2} \times 100 \quad (1)$$

Regions of interest (ROIs) for the spleen, thoracic spinal cord and femur (on the left and right hindlimb) were drawn manually on the structural images (MSOT image corresponding to 850 nm excitation) over the Z-stack. ImageJ (NIH, USA) was used for ROI analysis using the mouse atlas as a reference. The spinal cord and femur structures are clearly visible due to the bone structure (boundary) on the 850 nm structural MSOT image. Since we started the measurement around approximately the 5th rib, the relative slices where the spleen and femur could be present could be roughly estimated as the axial movement gap during image acquisition was preset at 0.3 mm. The spleen shows a continuous higher intensity structure on the 850 nm MSOT image and thus can be separated from the surroundings in the abdomen of the mouse. Next, we transferred the ROI set over the Z-stack to the corresponding computed sO_2 image from the same animal to extract the regional sO_2 value from each slice over the Z-stack that the organ is presented. Three independent ROI delineations over 30–40 horizontal slices were performed. The mean sO_2 value was calculated with the values from the Z-stack from three analyses. The volumes of the spleen were calculated based on known axial movement gaps during image acquisition (distance between slices = 0.3 mm) and the area drawn over each 2D horizontal image.

In addition, line profile analysis was performed to compare the signal intensity of different reconstruction methods (NNMB and MB) on the acquired 2D horizontal image (Fig. 2). Images with spleen and spinal cord presence were chosen.

2.7. FACS analysis of BM, spleen and blood

Murine femurs were harvested through careful dislocation at the joints between the hipbones and the knee and cleaned thoroughly of surrounding connective tissue and muscle using paper tissues. For FACS measurement, animals from eight naïve, nine sham and six tMCAO mice were examined. Murine spleens were extracted by abdominal incision. All organs were preserved in FACS buffer on ice before further processing. In turn, blood was collected immediately after euthanasia via intracardiac puncture using a 5 ml syringe and a 25 G needle. The samples were immediately transferred into a potassium ethylenediamine tetra-acetic acid (K^+ EDTA) blood collection tube and shaken vigorously for 15 s to avoid coagulation.

For the generation of single-cell suspensions, bones were crushed in 5 ml of FACS buffer (phosphate buffered saline with 2% fetal bovine serum and 2 mM EDTA), and the released cellular content was disaggregated via resuspension using a pipette. The cell suspensions were then filtered through a 70 μm cell strainer into a 50 ml collection tube. Bones were crushed as described three times to maximize marrow extraction and until bone fragments appeared completely pale. Spleens were crushed in FACS buffer directly into a 70 μm cell strainer using a syringe plunger under repeated washing. For the BM and spleen, red blood cells (RBCs) were removed by lysis in 2 ml of RBC lysis buffer (BioLegend) for 3 min. In the case of blood, 100 μl samples were lysed on 3 ml of RBCs for 3 min, and the reactions were inactivated through the addition of excess FACS buffer. Cells were then centrifuged, washed, and filtered once more before immunostaining for FACS analysis. Cells were then resuspended in fixed volumes, and the samples were blocked using Fc Receptor Blocking Solution (TruStain FcX™) at 4 °C. Cocktails of fluorescently labelled antibodies were added (STable 2), and the cells were incubated for 30 min at 4 °C. Cells were then washed twice in FACS buffer, resuspended in FACS buffer containing 4′,6-diamidino-2-phenylindole (DAPI; 0.5 μg/ml), and analysed on an LSR II Fortessa (BD Biosciences). Data analysis was performed using FlowJo software, version 10.8.

2.8. 2,3,5-Triphenyltetrazolium chloride (TTC) staining, spleen size and mass measurement

Staining with 2,3,5-triphenyltetrazolium chloride (TTC) was used to assess ischemic lesion severity in four sham and four tMCAO mice as previously described [42]. Mice were euthanized, their brains were removed, and 1 mm thick brain slices were obtained with a brain matrix (World Precision Instruments). Slices were incubated in a 2.5% TTC solution (Sigma–Aldrich, Switzerland) in 1 ×phosphate-buffered saline (PBS, pH 7.4) at 37 °C for 3 min. Photographs of the brain sections were taken. The spleens of six naïve, six sham and nine tMCAO mice were dissected and measured using a ruler and weighed.

2.9. Statistics

For data analysis, GraphPad Prism (GraphPad Prism 9.2.0, USA) and RStudio (R Core Team, Austria) [48] were used. An unpaired two-tailed t test was used for the comparison of regional [^{18}F]FDG SUV between the sham and tMCAO groups. One-way ANOVA with Sidak post hoc analysis was used for MSOT-derived sO_2, splenic volume, mass comparisons and

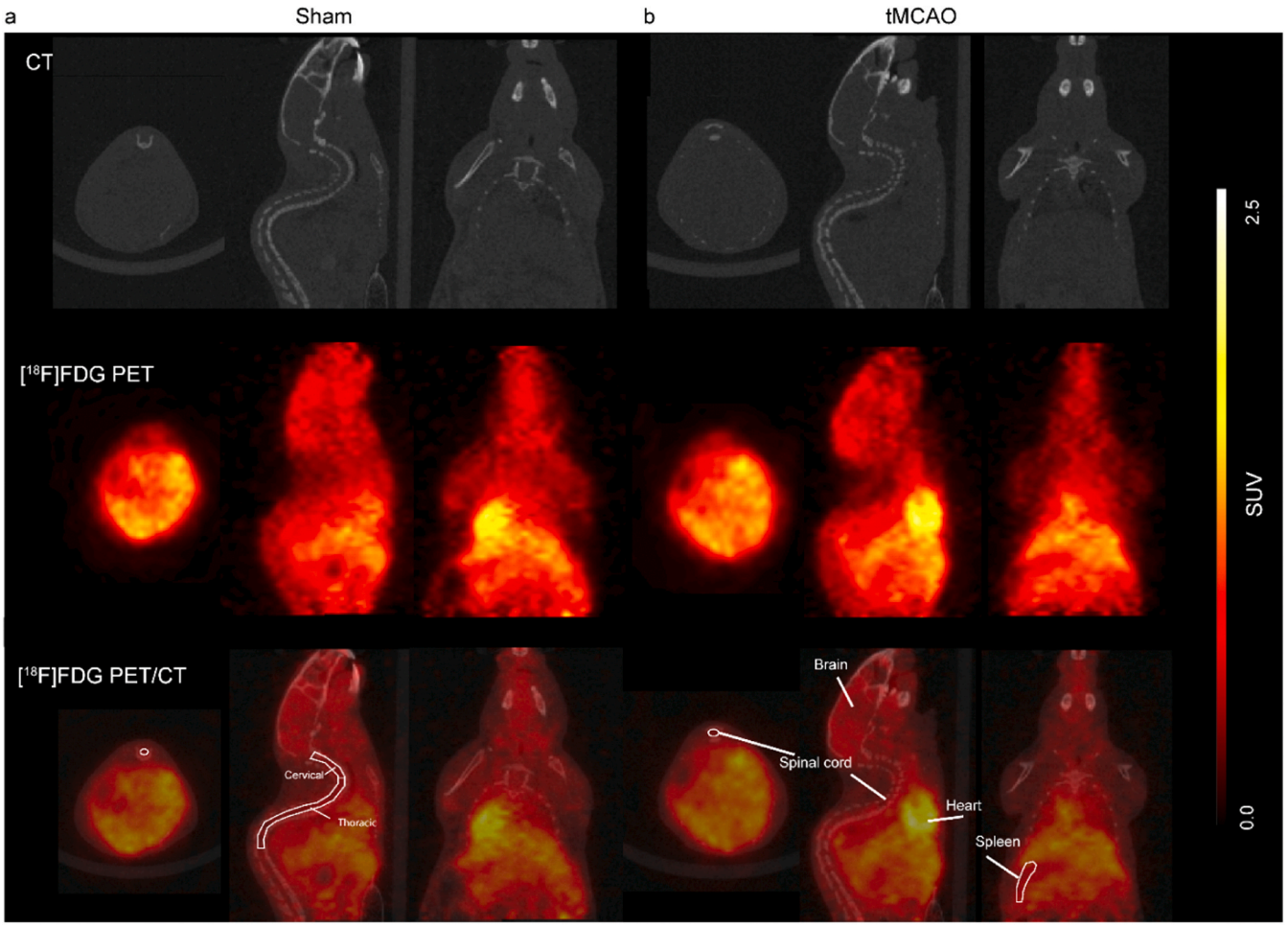

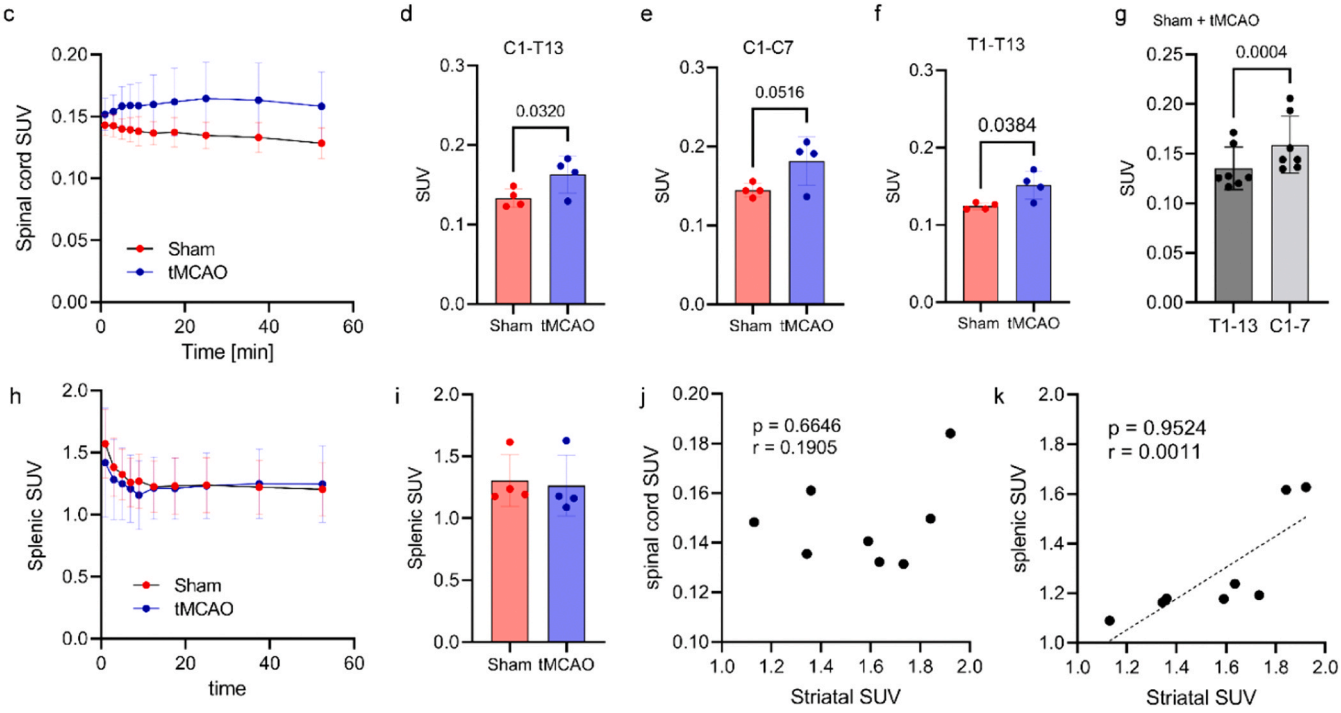

(caption on next page)

Fig. 1. *In vivo* [^{18}F]FDG PET of metabolism in the spleen of sham and tMCAO mice at 24 h after occlusion. (a, b) Representative axial, sagittal, and coronal views of [^{18}F]FDG uptake (Bq/ml) in sham-operated and tMCAO mice (n = 4 per group, averaging 18–53.5 min); CT, computed tomography. Spleen and spinal cord (including cervical and thoracic) regions of interest delineation are shown on [^{18}F]FDG PET-CT images. (c, h) Time activity curve of [^{18}F]FDG in the spinal cord and spleen of sham-operated and tMCAO mice. The volumes of interest for the spleen and spinal cord were manually delineated (white line for spleen). Difference in the spinal cord TAC between sham and tMCAO (mixed effect model treatment, p = 0.0399, treatment x time p = 0.0073). (d-f) The [^{18}F]FDG SUV signal was higher in the spinal cord (C1-T13, and C1–7, T1–13) of tMCAO mice compared to sham-operated mice. (g) The SUV is higher in C1–7 than in T1–13 of sham-operated + tMCAO mice. (i) No difference in [^{18}F]FDG SUV (n = 4 per group, averaging 18–53.5 min) in spleen FDG in sham-operated and tMCAO mice was detected. (j-k) No correlation between striatal and spinal cord [^{18}F]FDG SUV. (**i**) Positive correlation between striatal and splenic [^{18}F]FDG SUV (Spearman's rank analysis). Data are presented as the mean ± standard deviation (SD).

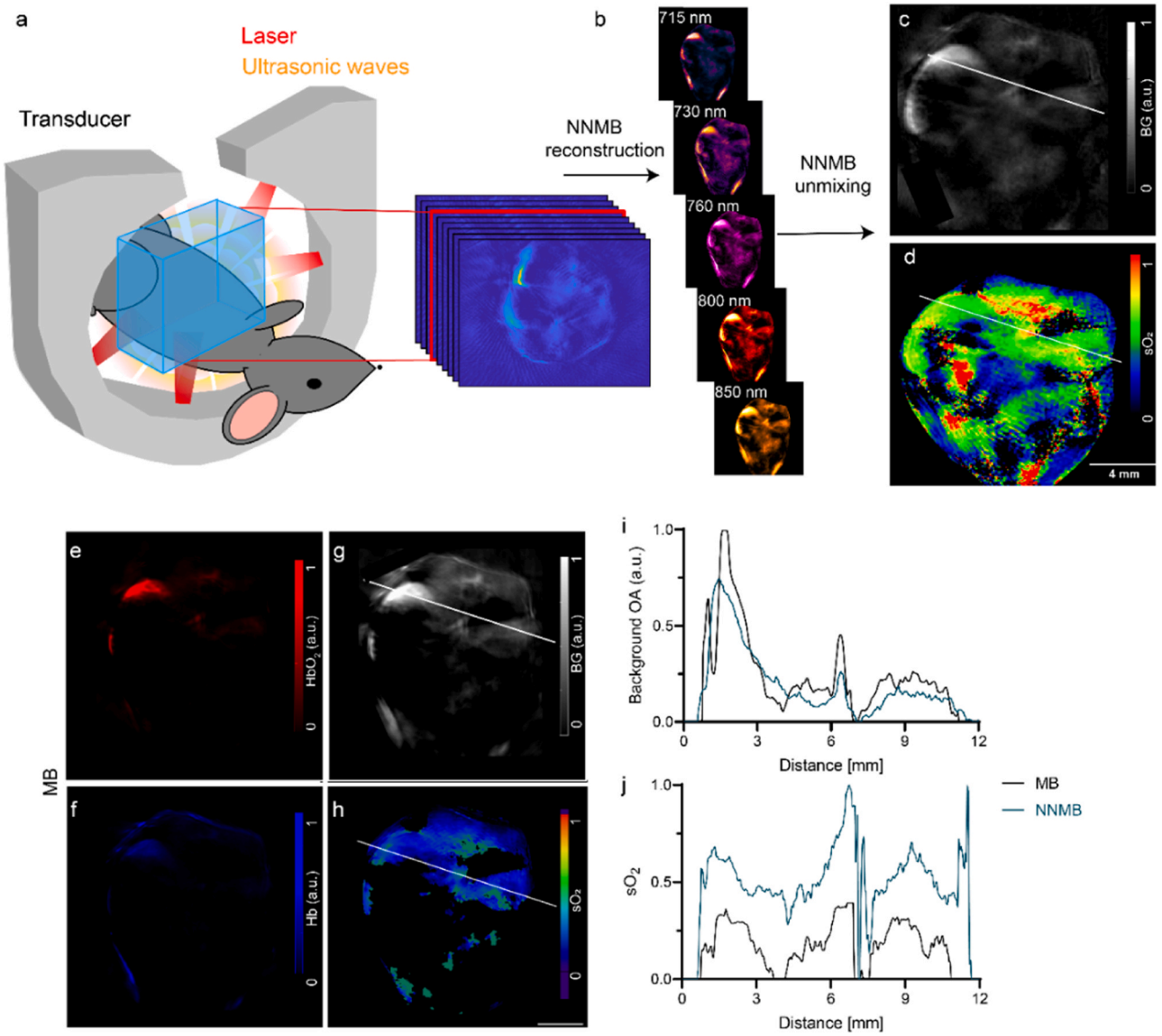

Fig. 2. *In vivo* MSOT of the mouse body and data processing. (a) Setup of the MSOT system for imaging across the mouse body; (b) non-negative model-based (NNMB) reconstructions of the *in vivo* vMSOT data for five distinct excitation wavelengths (715–850 nm). (c, d) Horizontal views of a background anatomy and oxygen saturation rate (sO_2) slice resulting from NNMB unmixing. Scale bar = 4 mm. (e-h) Same set of image data after standard model-based (MB) reconstruction and unmixing, HbO_2 (red), Hb (blue), background anatomy, and sO_2 slice. (i-j) Profile analysis of c, d and g, h showed differences in the background OA intensity and in sO_2 values processed by the MB and NNMB methods.

flow cytometry readouts between the three groups. Two-way ANOVA was used to compare the time course between groups. Spearman's rank correlation analysis was used to analyse the link between the [^{18}F]FDG SUV and sO_2 in the brain, spinal cord and spleen. Data are presented as the mean ± standard deviation (SD). Significance was set at $p < 0.05$.

3. Results

3.1. Focal cerebral ischemia leads to increased metabolism in the spinal cord

To investigate metabolic activity changes in the spinal cord and spleen due to tMCAO surgery, tMCAO and sham-operated mice

underwent [^{18}F]FDG PET at 24 h after reperfusion (Fig. 1). The time activity curves of [^{18}F]FDG uptake in the spleen and spinal cord of the sham and tMCAO groups are shown in Fig. 1c, h, and SFig. 1. We found an approximately 20% increase in [^{18}F]FDG uptake (average 18–53.5 min) in the spinal cord (C1-T13) of tMCAO mice (0.16 ± 0.02, n = 4) compared to sham-operated mice (0.13 ± 0.01, n = 4, p = 0.032, unpaired two-tailed t test) (Fig. 1d). Next, we further quantified [^{18}F]FDG uptake in cervical (C1–7) and thoracic (T1–13) spinal cord segments (Fig. 1e, f). [^{18}F]FDG uptake (averaged 18–53.5 min) was not different in the cervical part of the spinal cord of tMCAO mice (0.18 ± 0.03, n = 4) compared to sham-operated mice (0.14 ± 0.01, p = 0.0516, unpaired two-tailed t test) (Fig. 1e). In contrast, higher [^{18}F]FDG uptake (averaged 18–53.5 min) was observed in the thoracic part (T1–13) of tMCAO mice (0.151 ± 0.02, n = 4) than in sham-operated mice (0.124 ± 0.004, p = 0.0384, unpaired two-tailed t test) (Fig. 1f). In addition, [^{18}F]FDG uptake in the cervical part was higher than that in the thoracic part (0.16 ± 0.03 vs 0.14 ± 0.02, p = 0.0004, unpaired two-tailed t test) (Fig. 1g). There were no differences in splenic [^{18}F]FDG SUV uptake (averaged 18–53.5 min) in tMCAO mice (1.23 ± 0.01, n = 4) and sham-operated mice (1.22 ± 0.02, n = 4) at 24 h after occlusion (Fig. 1i). To examine whether there is a potential link between the brain and peripheral [^{18}F]FDG uptake, Spearman's rank analysis was performed between different readouts. There was a positive correlation between the ipsilateral striatal and splenic [^{18}F]FDG SUV (averaged 18–53.5 min, p = 0.0011 , r = 0.9524, Spearman's rank analysis). No correlation was observed between ipsilateral striatal and spinal cord [^{18}F]FDG SUV (Fig. 1j, k).

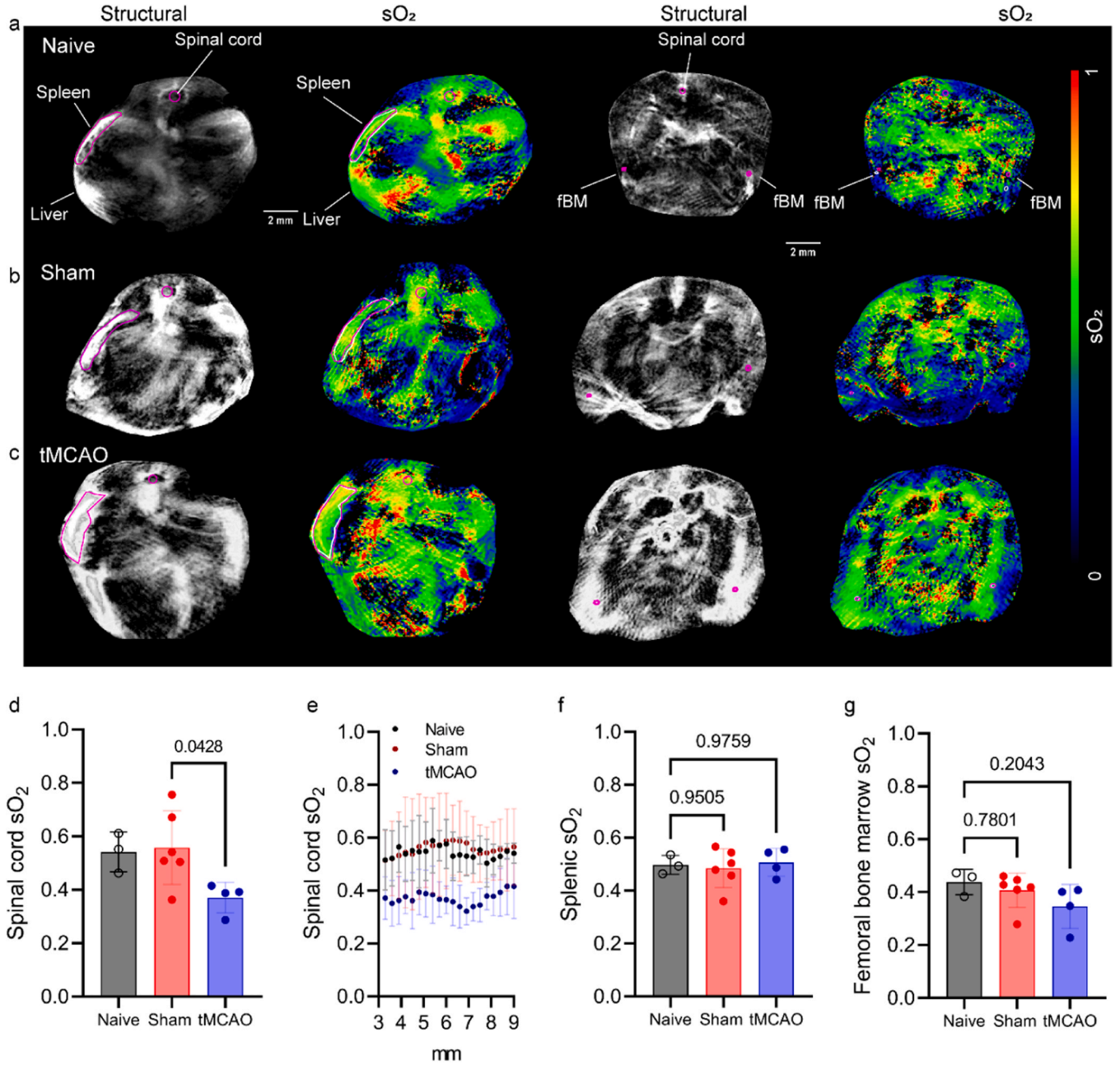

Fig. 3. *In vivo* MSOT of blood oxygenation in the spinal cord, spleen and femur of naïve, sham and tMCAO mice at 24 h after occlusion. (a-c) Oxygen saturation rate (sO_2) map in the spinal cord, spleen and femoral bone marrow (fBM) of naïve, sham-operated and tMCAO mice. (d, f, g) Reduced spinal cord oxygen saturation rate (sO_2) and comparable in the spleen and femoral bone marrow (fBM) of naïve (n = 3), sham-operated (n = 6) and tMCAO mice (n = 4). (e) Profile of sO_2 across different positions of the spinal cord. Data are presented as the mean ± standard deviation (SD).

3.2. NNMB reconstruction and unmixing

We used the MSOT system (Fig. 2a) for non-invasive visualization of the mouse body. The MSOT imaging pipeline consisted of reconstructing 3D images acquired at multiple excitation wavelengths (Fig. 2, SFig. 2) and spectral unmixing for different tissue chromophores, followed by manual ROI analysis. The reconstruction-unmixing processing steps are described in the methods section. The enhanced quantitative performance achieved with the NNMB method has been previously demonstrated in phantom studies [47] and in brain imaging data (orthotopic glioblastoma model) [49].

We compared the signal intensities of the images obtained with the custom-made NNMB reconstruction-unmixing framework with those of the images obtained with the standard MB approach integrated in the MSOT software package (Fig. 2b-h). The application of NNMB processing (reconstruction and unmixing) facilitated enhancing image features corresponding, e.g., to the spinal cord and the spleen as well as to other organs at deeper locations in the structural images and, to a greater extent, in the sO_2 images (indicated by the line profile analysis) (Fig. 2i, j).

3.3. Focal cerebral ischemia leads to reduced thoracic spinal cord oxygenation

To reveal oxygenation in the thoracic spinal cord and spleen after tMCAO *in vivo*, mice were assessed with MSOT at 24 h after occlusion. The spleen, cervical and thoracic spinal cord and femur in the representative structural map resulting from NNMB processing had clear boundaries and were used for ROI delineation and later transferred to sO_2 images for data analysis (Fig. 3a-c). In the thoracic spinal cord, the sO_2 of the tMCAO group (0.37 ± 0.06, $n = 4$) was lower than that of the sham-operated group (0.56 ± 0.14, $n = 6$, $p = 0.0428$, one-way ANOVA with Sidak post hoc analysis) (Fig. 3d). Variation in the sO_2 across the thoracic spinal cord was observed. Comparable sO_2 (one-way ANOVA with Sidak post hoc analysis) was detected in the spleen of naïve (0.5 ± 0.04, $n = 3$), sham-operated (0.5 ± 0.07, $n = 6$), and tMCAO mice (0.5 ± 0.05, $n = 4$) (Fig. 3f) and in the femur of naïve (0.4 ± 0.05, $n = 3$), sham-operated (0.5 ± 0.07, $n = 6$), and tMCAO mice (0.3 ± 0.08, $n = 4$) (Fig. 3g).

3.4. Alterations in hematopoietic and lymphoid organs after tMCAO

Flow cytometry analysis revealed major changes in hematopoietic and lymphoid organs, as well as circulating cells, after tMCAO and sham surgeries. In general, we observed that tMCAO led to a significant increase in the numbers of mature T cells (CD4 and CD8) in femoral BM tissues (Fig. 4e, f), concomitant with a stark reduction in these cell subsets in the spleen (Fig. 5e, f) and their decrease in peripheral blood (Fig. 6d, e) by using one-way ANOVA with Sidak post hoc analysis. In turn, the numbers of mature granulocytes (determined as $CD11b^{+}Gr1^{hi}$ cells) decreased in BM tissues (Fig. 4b) and blood (Fig. 6a) but increased in the spleen (Fig. 5b) by using one-way ANOVA with Sidak post hoc analysis. Notably, both trends were also observed to a large extent in sham-operated mice. As previously reported, tMCAO induced subtle but significant increases in the frequencies and absolute numbers of hematopoietic progenitor cells ($Lin^{-}c\text{-}kit^{+}Sca\text{-}1^{+}$, LSK) (Fig. 4g, n) and HSCs ($LSKCD48^{-}CD150^{+}$) (Fig. 4h, o). Again, alterations in these early primitive hematopoietic progenitors were also found, albeit at lower magnitudes, in sham controls (Fig. 4c, j). This suggests that the profound redistribution of mature cell types from peripheral circulation and spleen to BM tissues as well as the reactive expansions of early progenitor populations and HSCs are largely caused by surgery-associated stress and accentuated in mice subjected to tMCAO.

3.5. Histology and TTC staining validation and spleen pathology

Significantly reduced weight in both sham-operated (22.1 ± 2.1 g, $p = 0.0425$) and tMCAO mice (21.6 ± 2.0 g, $p = 0.0054$) was detected compared to naïve mice (25.6 ± 1.3 mg, $p = 0.0029$, one-way ANOVA with Sidak post hoc analysis). Ischemic lesions in the tMCAO mice were validated by the presence of nonviable tissue white areas shown by TTC staining (approximately 42%, Fig. 7a, d). The spleens of the sham-operated and tMCAO mice were dissected, and the splenic size and mass were measured after *in vivo* imaging (Fig. 7b, c). Compared to naïve mice (88.7 ± 31.7 mg, $n = 6$), reduced splenic mass at approximately 25 h after reperfusion (after *in vivo* imaging) was detected in both the sham and tMCAO mice (Fig. 7e, one-way ANOVA with Sidak post hoc analysis). No difference in the *ex vivo* splenic size was detected between sham and tMCAO mice.

4. Discussion

Here, we demonstrated non-invasive imaging of increased metabolism and reduced oxygen saturation in the spinal cord but not in the spleen of tMCAO mice at 24 h after 1 h of occlusion. We observed increased [^{18}F]FDG uptake in the spinal cord (C1-T13 and thoracic T1–13) and that the uptake was higher in the cervical than in the thoracic part of the mice. This may be because the cervical (~C4–6) and lumbar (~T11-L1) enlargements for limb control have more grey matter than other sections of the spinal cord [50]. A previous [^{18}F]FDG study in the human spinal cord showed that [^{18}F]FDG uptake is lower in the mid-thoracic spine than in other sections under physiological conditions [51]. [^{18}F]FDG PET has demonstrated a reduced cerebral metabolic rate for glucose after permanent MCAO and tMCAO in rats [52,53] and mice [54]. In the spinal cord, [^{18}F]FDG PET has indicated increased glycolysis and metabolic changes in EAE mice, rats with inflammatory infiltrates [43,55,56], transgenic Parkinson's disease mice [57], tumor models [58], and animal models after injuries and immune responses [59–62]. In healthy human subjects, [^{18}F]FDG PET/CT showed a decreasing pattern from cervical to lumbar vertebrae and peaked at C4–6 and T12 [63–65]. In patients with acute myocardial infarction, [^{18}F]FDG-PET measures of metabolic activity were significantly higher in the BM lumbar spinal cord [26,27] and spleen and were associated with an increased risk of cardiovascular events [66,67].

MicroPET imaging has limitations in detecting functional or molecular changes in small animals due to its suboptimal spatial resolution (1.6–1.7 mm) in comparison to other mesoscale modalities, such as MSOT (100–200 μm), as well as the spill-over effect. Thus, given the small size of the femur BM of the mice, we did not analyse the [^{18}F]FDG uptake in the femur BM. Due to the limited FOV of the PET scan, the mouse lumbar spinal cord was not covered in our study.

The NNMB algorithm provides reasonable values (between 0 and 1) across the entire section of the mouse. Note that unconstrained reconstruction leads to negative values that have no meaning. On the other hand, we have previously validated the NNMB approach by imaging optical probes within tubing inserted in a mouse [68]. In this case, the concentrations of the probes are known and can be taken as a reference. We found that the NNMB approach provides more quantitative unmixing and thus is also expected to provide more quantitative sO_2 values. Notably, bones can lead to ultrasound propagation aberrations causing strong image distortion. However, the effects of the murine bones for the typical resolution provided by MSOT systems (~150 μm for the system used in this study) are not very significant. Indeed, we have repeatedly used 3D MSOT to image the brain through the murine skull bone [69–71], which causes stronger aberrations than, e.g., the spinal cord. Considering that algorithms [72,73] that can mitigate the effects of acoustic distortions and speed of sound changes in the spinal cord can only lead to a marginal improvement, we opted to use the NNMB approach for reconstruction, which has a larger impact on sO_2 readings.

We demonstrated reduced MSOT sO_2 (indicating hypoxia) in the

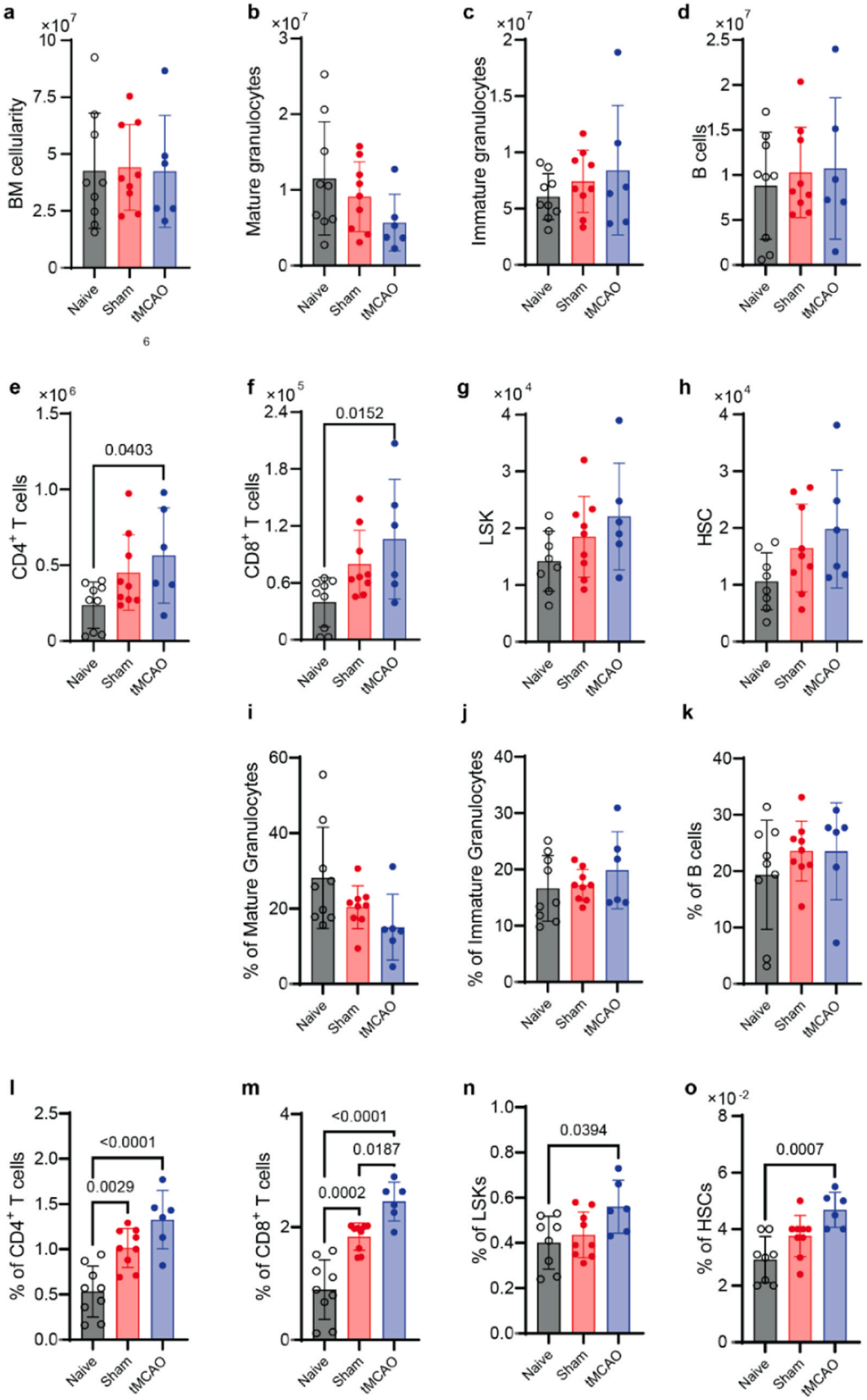

Fig. 4. tMCAO increased the numbers of mature T cells in femur bone marrow. Flow cytometric analysis of the absolute number (a-h) and percentage (i-o) of mature granulocytes, immature granulocytes, B cells, CD4 + T cells, CD8 + T cells, LSCs and HSCs in the femur bone marrow of naïve (n = 8), sham-operated (n = 9) and tMCAO mice (n = 6). Data are presented as the mean ± standard deviation (SD). One-way ANOVA with Sidak post hoc analysis.

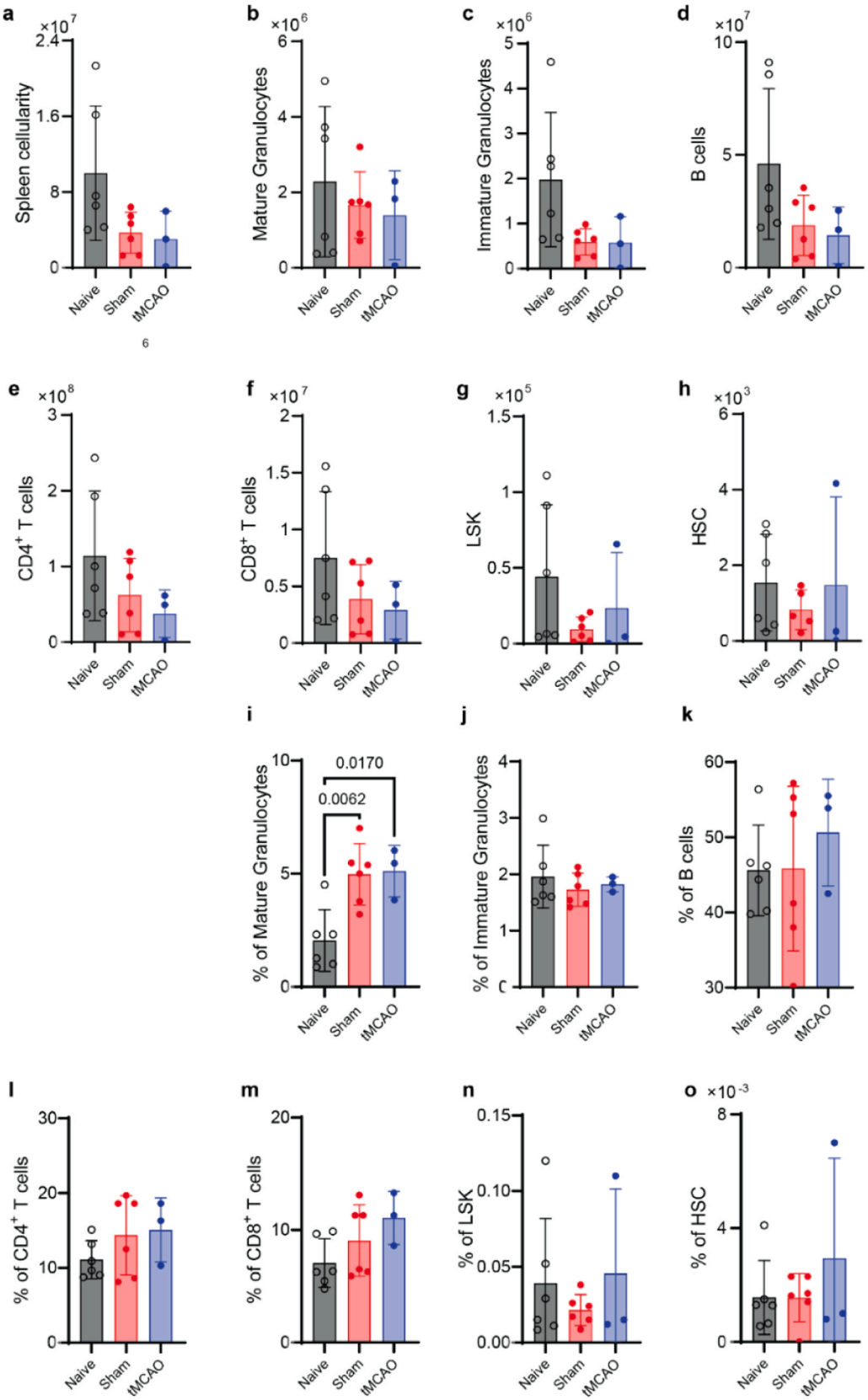

Fig. 5. tMCAO increased mature granulocytes in the spleen. Flow cytometric analysis of the absolute number (a-h) and percentage (i-o) of mature granulocytes, immature granulocytes, B cells, CD4 + T cells, CD8 + T cells, LSCs and HSCs in the spleen of naïve (n = 6), sham-operated (n = 6) and tMCAO mice (n = 3). Data are presented as the mean ± standard deviation (SD). One-way ANOVA with Sidak post hoc analysis.

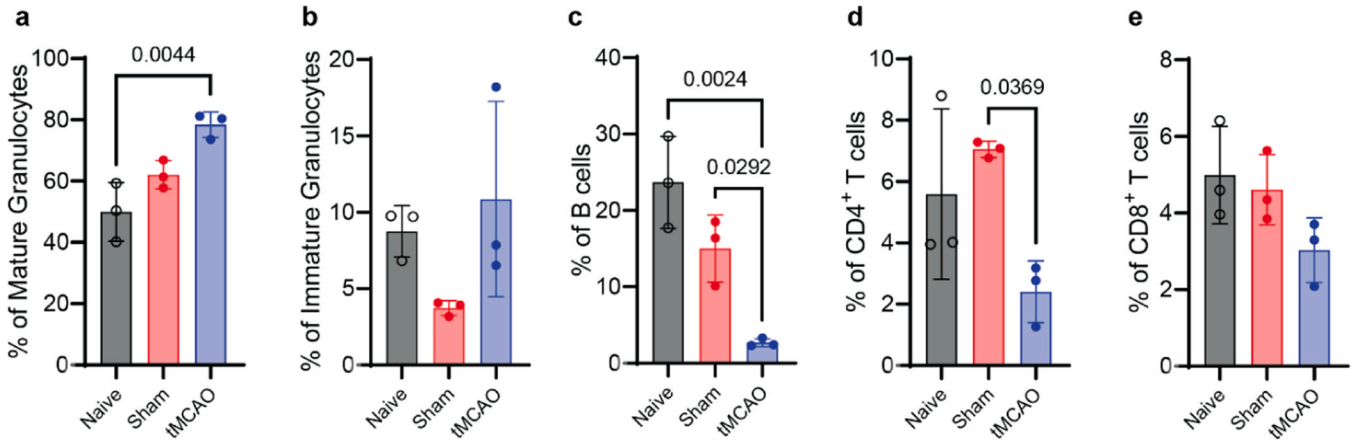

Fig. 6. tMCAO reduced B cells and T cells in circulating blood. Flow cytometric analysis showed (a) an increased percentage of mature granulocytes in circulating blood from tMCAO mice compared to that from naïve mice. (b) No difference in the percentage of immature granulocytes in circulating blood from naïve or sham mice with tMCAO mice. (c) Reduced percentage of B cells in circulating blood from tMCAO mice compared to naïve and sham mice. (d) Reduced percentage of CD4 + T cells in circulating blood from tMCAO mice compared to sham mice. (e) No difference in the percentage of CD8 + T cells in circulating blood from naïve, sham and tMCAO mice. n = 3 per group. Data are presented as the mean ± standard deviation (SD). One-way ANOVA with Sidak post hoc analysis.

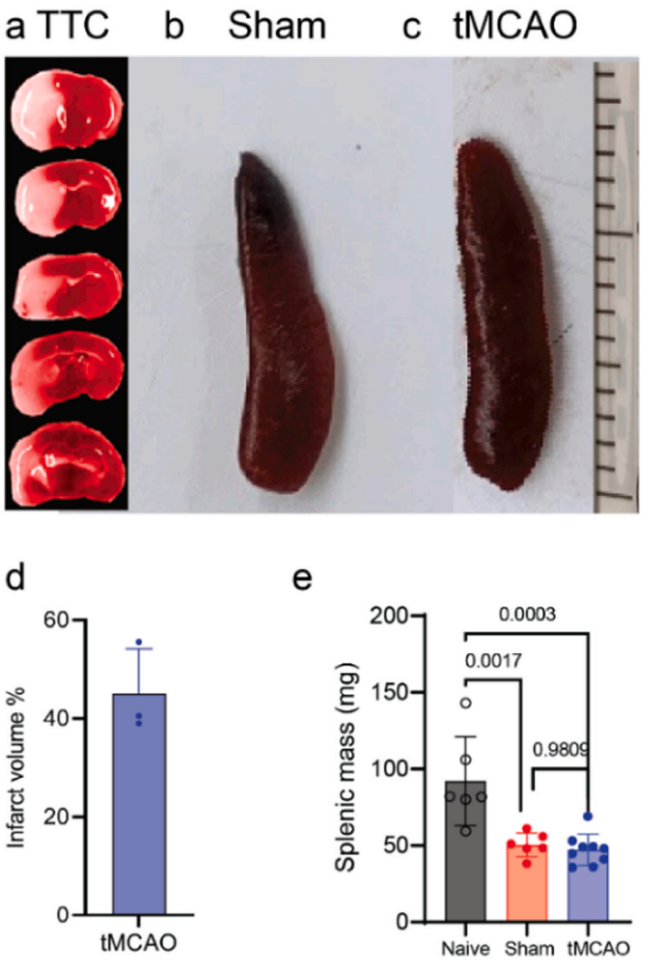

Fig. 7. Assessment of the spleen volume and histology of the brain and spleen of sham and tMCAO mice at 24 h after occlusion. (a) TTC of tMCAO mouse brain slices indicating lesions in the ipsilateral striatum and cortex. (b, c) Representative images of dissected spleens from sham-operated and tMCAO mice. (d) Percentage of infarct volume in the brains of tMCAO mice. (e) Reduced mass of dissected spleen among naïve (n = 6), sham-operated (n = 6) and tMCAO mice (n = 9) *ex vivo*. Data are presented as the mean ± standard deviation (SD).

spinal cord of tMCAO mice compared to sham-operated mice. Oxygen availability varies among tissues and sites within the same tissue. Local tissue oxygen tension is shown to be one physiological regulatory mechanism of immune responses [22]. A recent study showed a novel oxygen sensing mechanism in the spinal cord involved in cardiorespiratory responses to hypoxia [74]. Stroke increases sympathetic nervous activity in the BM of the tMCAO mouse model [4]. tMCAO induces dynamic secondary degeneration [75,76] and rapid activation of the peripheral immune system in the spinal cord, as well as blood–spinal cord barrier alterations in rodents [16,18–20]. High-field magnetic resonance imaging has been used to detect oxygen metabolism in the brains of stroke patients and animal models [77–80]. Recent MSOT studies in animal models have demonstrated spinal cord hypoxia in experimental autoimmune encephalomyelitis (EAE) models [81] and white matter loss in a spinal cord injury model [82] and enabled the monitoring of image-guided stem cell therapy [83–86]. A recent study showed the feasibility of MSOT imaging of hyperoxia in the femur BM of a leukaemia animal model [87]. Here, we did not observe a difference in the MSOT sO_2 of femur BM between tMCAO mice and sham-operated mice due to the variability and small ROI size.

The spleen is a hematopoietic organ and an immediate reservoir of monocytes [6,88]. The spleen may respond to injury in the brain by releasing stored immune cells into the blood, infiltrating into the brain and promoting a secondary inflammatory response [43]. Increased [^{18}F]FDG uptake has not been reported in spleen ischemic stroke patients compared to controls [8]. Previous studies in animal models have demonstrated altered splenic function after ischemic stroke and increased levels of circulating proinflammatory cytokines [11–13,89]. We observed no difference in splenic [^{18}F]FDG uptake between tMCAO and sham-operated mice, while there was a positive association between [^{18}F]FDG uptake in the ipsilateral striatum and spleen. In addition, we observed similar splenic sO_2 in tMCAO mice at 24 h after occlusion compared to sham-operated mice. The splenic oxygen levels vary between 0.5% and 4.5%, depending on the distance from the splenic artery [90].

We found a decrease in splenic mass in tMCAO mice 24 h after occlusion compared to naïve mice but not to sham-operated mice *ex vivo*. In addition, tMCAO led to a significant increase in the numbers of mature T cells in femoral BM tissues, concomitant with a stark reduction in these cell subsets in the spleen and their decrease in peripheral blood, while the numbers of mature granulocytes decreased in BM and blood and increased in the spleen. This is in line with previous reports of spleen weight reductions in mice after tMCAO [13–15], accompanied by a

decreased number of monocytes/macrophages in the spleen [26,27] and increased myeloid cells [8,41]. Splenic atrophy was also reported in permanent MCAO in rats at 24 h [11] and at 4 days [91]. However, some studies did not include sham (surgery, but no ischemic brain injury) controls [14,15]. Myeloid cells are trafficked to the ischemic brain, where they participate in the inflammatory response [9,15]. Several studies have reported splenic atrophy and decreased monocytes at 4 days [13], 3–7 days [92], and 3h-7 days [10] after tMCAO in mice. The number of mature T cells in the spleen and blood decreased and showed reduced interferon-γ production in tMCAO mice from 24 h to 14 days [93]. An earlier study showed that tMCAO increased monocyte/macrophage subsets at 3 and 7 days after ischemia in the BM, as well as an increase in circulation [15]. In addition, tMCAO activates BM HSCs and downstream hematopoietic progenitors, leading to an increased output of inflammatory monocytes and neutrophils in an animal model [4], whereas the number of lymphocyte progenitors declined. We did not observe an additional effect of cerebral ischemia on the deployment of cells from the spleen in our study. Our spleen volume and FACS data suggest that the experimental intervention dominates the egress of splenic cells into the circulation. The examination time point after occlusion and the animal model used might contribute to the different observations between studies.

In patients with acute stroke, spleen sizes were measured with abdominal ultrasound, and a statistically significant negative association was also observed between the pattern of change in total white blood cell count and spleen volume [94]. Splenic volume reduction is associated with poststroke infection in patients [95]. Using abdominal computed tomography, another study revealed that stroke induced an initial reduction (until 48 h) followed by an increase in the splenic volume in patients [96].

It is noted that there is a possibility that ECA/ICA ligation may cause ischemia to the cervical sympathetic chain and associated ganglia (superior cervical ganglia) since the left common carotid artery, the external carotid artery and the internal carotid artery are ligated in the course. Ischaemia has been shown to produce an increase in thoracic sympathetic chain activity that persists after transection at both the ponto-medullary and medullary-spinal cord levels [97]. Cervical sympathetic trunk ischemia induced by bilateral common carotid artery ligation has been shown to lead to degeneration of the cervical sympathetic trunk, which inhibits sympathetic activity [98]. Cervical sympathetic trunk transection has been shown to lead to a decreased inflammatory response [99]. This would argue that cervical sympathetic trunk ischemia due to the tMCAO procedure should lead to a decrease in sympathetic activity and reduced hematopoietic bone marrow stem cell activity. However, this is not the case in a previous report where MCAO mice showed increased sympathetic nervous system activity, which modulated the hematopoietic bone marrow environment and thereby contributed to the elevation of inflammatory cells after cerebral ischemia [4].

There are several limitations in the current study. First, fluence correction is expected to further improve the accuracy of the signal at depth, which was not performed in the current study [100]. Second, regarding animal models and sample size: sham operation might also introduce inflammatory response and increased proportion of circulating neutrophils in the blood of animal [7]. [^{18}F]FDG uptake has been shown associated with neutrophils and inflammatory response in earlier studies in other disease models [101]. However we did not perform [^{18}F]FDG PET comparing sham-operated and tMCAO mice to the naïve mice in the current study. In addition, postischemic stroke inflammation and metabolic changes are dynamic processes [102]. Sex differences and age-related factors also influence ischemic stroke sensitivity [103]. Therefore, further study including additional naïve mice as a negative control, female and male aged mouse groups for a longer time frame is needed to dissect the effect of cerebral ischemic lesions from confounding factors induced by the tMCAO procedure, including the cervical sympathetic trunk, on the hematopoietic system. Third, due to the complications in experimental procures, the number of tissue sample extracts was not exactly matched for FACS analysis. Fourth, regarding imaging techniques, oxygen levels vary within the same tissue [90]; however, the resolution of the PET and MSOT systems used here is not sufficient to dissect different compartments in the BM and spleen of mice. The image quality will be further improved with MSOT having a 256-element transducer array [104–106] and transmission–reflection optoacoustic ultrasound computed tomography [107] compared to the one with the 128 element transducer array used in the current study. In addition, anaesthesia and mild surgical manipulation may induce granulocyte mobilization and systemic cytokine induction [108], which needs to be further elucidated.

In conclusion, we demonstrated increased metabolic activity in the spinal cord by non-invasive multimodal imaging in tMCAO mice. The inflammatory linkage among the BM, spleen, and blood after acute cerebral ischemia needs to be further investigated. A bidirectional relationship between hypoxia and inflammation has been demonstrated in ischemic stroke (hypoxia-induced inflammation, or inflammation reduced the rate of oxygen delivery to tissues and elicited hypoxic conditions) [109].

Funding

JK received funding from the Swiss National Science Foundation (320030_179277) in the framework of ERA-NET NEURON (32NE30_173678/1), the Synapsis Foundation, the Olga Mayenfisch Stiftung, and the Vontobel Foundation. RN received funding from Helmut Horten Stiftung and University of Zurich [MEDEF-20-021].

CRediT authorship contribution statement

RN and JK designed the study; LM, RN, GL, SF, CA, and JK performed the experiment; RN, NS, XLDB, LM, SF, CA, and JK performed the analysis; RN and JK wrote the draft. All authors read and approved the final manuscript.

Declaration of Competing Interest

The authors declare that they have no known competing financial interests or personal relationships that could have appeared to influence the work reported in this paper.

Data availability

Data will be made available on request.

Acknowledgements

The authors acknowledge Prof. Roger Schibli and Annette Krämer at the Center for Radiopharmaceutical Sciences, Department of Chemistry and Applied Biosciences, ETH Zurich, and Ms. Diana Kindler at the Institute for Biomedical Engineering, ETH Zurich.

Appendix A. Supporting information

Supplementary data associated with this article can be found in the online version at doi:10.1016/j.pacs.2023.100532.

References

[1] K. Prass, C. Meisel, C. Höflich, J. Braun, E. Halle, T. Wolf, K. Ruscher, I. V. Victorov, J. Priller, U. Dirnagl, H.D. Volk, A. Meisel, Stroke-induced immunodeficiency promotes spontaneous bacterial infections and is mediated by sympathetic activation reversal by poststroke T helper cell type 1-like immunostimulation, J. Exp. Med 198 (5) (2003) 725–736.

[2] U. Dirnagl, J. Klehmet, J.S. Braun, H. Harms, C. Meisel, T. Ziemssen, K. Prass, A. Meisel, Stroke-induced immunodepression: experimental evidence and clinical relevance, Stroke 38 (2 Suppl) (2007) 770–773.

[3] A. Wunder, J. Klohs, U. Dirnagl, Non-invasive visualization of CNS inflammation with nuclear and optical imaging, Neuroscience 158 (3) (2009) 1161–1173.

[4] G. Courties, F. Herisson, H.B. Sager, T. Heidt, Y. Ye, Y. Wei, Y. Sun, N. Severe, P. Dutta, J. Scharff, D.T. Scadden, R. Weissleder, F.K. Swirski, M.A. Moskowitz, M. Nahrendorf, Ischemic stroke activates hematopoietic bone marrow stem cells, Circ. Res 116 (3) (2015) 407–417.

[5] C. Iadecola, J. Anrather, The immunology of stroke: from mechanisms to translation, Nat. Med 17 (7) (2011) 796–808.

[6] F.K. Swirski, M. Nahrendorf, M. Etzrodt, M. Wildgruber, V. Cortez-Retamozo, P. Panizzi, J.L. Figueiredo, R.H. Kohler, A. Chudnovskiy, P. Waterman, E. Aikawa, T.R. Mempel, P. Libby, R. Weissleder, M.J. Pittet, Identification of splenic reservoir monocytes and their deployment to inflammatory sites, Science 325 (5940) (2009) 612–616.

[7] M. Vaas, G. Enzmann, T. Perinat, U. Siler, J. Reichenbach, K. Licha, A. Kipar, M. Rudin, B. Engelhardt, J. Klohs, Non-invasive near-infrared fluorescence imaging of the neutrophil response in a mouse model of transient cerebral ischaemia, J. Cereb. Blood Flow. Metab. 37 (8) (2017) 2833–2847.

[8] S. Wattananit, D. Tornero, N. Graubardt, T. Memanishvili, E. Monni, J. Tatarishvili, G. Miskinyte, R. Ge, H. Ahlenius, O. Lindvall, M. Schwartz, Z. Kokaia, Monocyte-derived macrophages contribute to spontaneous long-term functional recovery after stroke in mice, J. Neurosci. 36 (15) (2016) 4182–4195.

[9] J. Klohs, M. Gräfe, K. Graf, J. Steinbrink, T. Dietrich, D. Stibenz, P. Bahmani, G. Kronenberg, C. Harms, M. Endres, U. Lindauer, K. Greger, E.H. Stelzer, U. Dirnagl, A. Wunder, In vivo imaging of the inflammatory receptor CD40 after cerebral ischemia using a fluorescent antibody, Stroke 39 (10) (2008) 2845–2852.

[10] E. Kim, J. Yang, C.D. Beltran, S. Cho, Role of spleen-derived monocytes/macrophages in acute ischemic brain injury, J. Cereb. Blood Flow. Metab. 34 (8) (2014) 1411–1419.

[11] M. Vendrame, C. Gemma, K.R. Pennypacker, P.C. Bickford, C. Davis Sanberg, P. R. Sanberg, A.E. Willing, Cord blood rescues stroke-induced changes in splenocyte phenotype and function, Exp. Neurol. 199 (1) (2006) 191–200.

[12] H. Offner, S. Subramanian, S.M. Parker, M.E. Afentoulis, A.A. Vandenbark, P. D. Hurn, Experimental stroke induces massive, rapid activation of the peripheral immune system, J. Cereb. Blood Flow. Metab. 26 (5) (2006) 654–665.

[13] H. Offner, S. Subramanian, S.M. Parker, C. Wang, M.E. Afentoulis, A. Lewis, A. A. Vandenbark, P.D. Hurn, Splenic atrophy in experimental stroke is accompanied by increased regulatory T cells and circulating macrophages, J. Immunol. 176 (11) (2006) 6523–6531.

[14] Y. Bao, E. Kim, S. Bhosle, H. Mehta, S. Cho, A role for spleen monocytes in post-ischemic brain inflammation and injury, J. Neuroinflamm. 7 (2010) 92.

[15] E. Kim, J. Yang, C.D. Beltran, S. Cho, Role of spleen-derived monocytes/macrophages in acute ischemic brain injury, J. Cereb. Blood Flow. Metab. 34 (8) (2014) 1411–1419.

[16] S. Garbuzova-Davis, E. Haller, N. Tajiri, A. Thomson, J. Barretta, S.N. Williams, E. D. Haim, H. Qin, A. Frisina-Deyo, J.V. Abraham, P.R. Sanberg, H. Van Loveren, C. V. Borlongan, Blood-spinal cord barrier alterations in subacute and chronic stages of a rat model of focal cerebral ischemia, J. Neuropathol. Exp. Neurol. 75 (7) (2016) 673–688.

[17] B. Huang, Q. Xie, X. Lu, T. Qian, S. Li, R. Zhu, W. Yu, G. Chen, Z. Chen, X. Xu, T. Wang, L. Li, GlyT1 inhibitor NFPS exerts neuroprotection via GlyR Alpha1 subunit in the rat model of transient focal cerebral ischaemia and reperfusion, Cell. Physiol. Biochem. 38 (5) (2016) 1952–1962.

[18] G. Dang, X. Chen, Y. Chen, Y. Zhao, F. Ouyang, J. Zeng, Dynamic secondary degeneration in the spinal cord and ventral root after a focal cerebral infarction among hypertensive rats, Sci. Rep. 6 (2016) 22655.

[19] K. Moisse, I. Welch, T. Hill, K. Volkening, M.J. Strong, Transient middle cerebral artery occlusion induces microglial priming in the lumbar spinal cord: a novel model of neuroinflammation, J. Neuroinflamm. 5 (2008) 29.

[20] G. Dang, X. Chen, Y. Zhao, Y. Chen, F. Ouyang, J. Liang, Y. Guo, J. Zeng, Alterations in the spinal cord and ventral root after cerebral infarction in non-human primates, Restor. Neurol. Neurosci. 36 (6) (2018) 729–740.

[21] K. Ito, T. Suda, Metabolic requirements for the maintenance of self-renewing stem cells, Nat. Rev. Mol. Cell Biol. 15 (4) (2014) 243–256.

[22] A. Ohta, R. Diwanji, R. Kini, M. Subramanian, A. Ohta, M. Sitkovsky, In vivo T cell activation in lymphoid tissues is inhibited in the oxygen-poor microenvironment, Front. Immunol. 2 (2011) 27.

[23] A. Lupi, G. Todeschini, P. Zanco, Diffuse metabolic activation of reticuloendothelium on F-18 FDG PET imaging in a case of visceral leishmania, Clin. Nucl. Med 31 (1) (2006) 34–36.

[24] G.G. Bural, D.A. Torigian, W. Chen, M. Houseni, S. Basu, A. Alavi, Increased 18F-FDG uptake within the reticuloendothelial system in patients with active lung cancer on PET imaging may indicate activation of the systemic immune response, Hell. J. Nucl. Med 13 (1) (2010) 23–25.

[25] M.A. Walter, R.A. Melzer, C. Schindler, J. Müller-Brand, A. Tyndall, E. U. Nitzsche, The value of [18F]FDG-PET in the diagnosis of large-vessel vasculitis and the assessment of activity and extent of disease, Eur. J. Nucl. Med Mol. Imaging 32 (6) (2005) 674–681.

[26] E.J. Kim, S. Kim, D.O. Kang, H.S. Seo, Metabolic activity of the spleen and bone marrow in patients with acute myocardial infarction evaluated by 18f-fluoro-deoxyglucose positron emission tomograpic imaging, Circ. Cardiovasc Imaging 7 (3) (2014) 454–460.

[27] B. Assmus, M. Iwasaki, V. Schächinger, T. Roexe, M. Koyanagi, K. Iekushi, Q. Xu, T. Tonn, E. Seifried, S. Liebner, W.T. Kranert, F. Grünwald, S. Dimmeler, A. M. Zeiher, Acute myocardial infarction activates progenitor cells and increases Wnt signalling in the bone marrow, Eur. Heart J. 33 (15) (2012) 1911–1919.

[28] J.M. Kim, E.S. Lee, K.Y. Park, J.W. Seok, Decreased (18F)-fluorodeoxyglucose uptake in lumbar vertebrae of stroke patients, J. Clin. Neurol. 17 (1) (2021) 41–45.

[29] D. Razansky, J. Klohs, R. Ni, Multi-scale optoacoustic molecular imaging of brain diseases, Eur. J. Nucl. Med. Mol. Imaging (2021).

[30] D. Razansky, A. Buehler, V. Ntziachristos, Volumetric real-time multispectral optoacoustic tomography of biomarkers, Nat. Protoc. 6 (8) (2011) 1121–1129.

[31] L.V. Wang, S. Hu, Photoacoustic tomography: in vivo imaging from organelles to organs, Science 335 (6075) (2012) 1458.

[32] R. Ni, M. Rudin, J. Klohs, Cortical hypoperfusion and reduced cerebral metabolic rate of oxygen in the arcAβ mouse model of Alzheimer's disease, Photoacoustics 10 (2018) 38–47.

[33] X.L. Deán-Ben, J. Robin, R. Ni, D. Razansky, Noninvasive three-dimensional optoacoustic localization microangiography of deep tissues, arXiv preprint arXiv: 2007.00372 (2020).

[34] C.B. Sussman, C. Rossignol, Q. Zhang, H. Jiang, T. Zheng, D. Steindler, L. Young, M.D. Weiss, Photoacoustic tomography can detect cerebral hemodynamic alterations in a neonatal rodent model of hypoxia-ischemia, Acta Neurobiol. Exp. 72 (3) (2012) 253–263.

[35] M. Kneipp, J. Turner, S. Hambauer, S.M. Krieg, J. Lehmberg, U. Lindauer, D. Razansky, Functional real-time optoacoustic imaging of middle cerebral artery occlusion in mice, PLoS One 9 (4) (2014), e96118.

[36] J. Lv, S. Li, J. Zhang, F. Duan, Z. Wu, R. Chen, M. Chen, S. Huang, H. Ma, L. Nie, In vivo photoacoustic imaging dynamically monitors the structural and functional changes of ischemic stroke at a very early stage, Theranostics 10 (2) (2020) 816–828.

[37] Y.H. Liu, S.J. Chan, H.C. Pan, A. Bandla, N.K.K. King, P.T.H. Wong, Y.Y. Chen, W. H. Ng, N.V. Thakor, L.D. Liao, Integrated treatment modality of cathodal-transcranial direct current stimulation with peripheral sensory stimulation affords neuroprotection in a rat stroke model, Neurophotonics 4 (4) (2017), 045002.

[38] X. Yang, Y.H. Chen, F. Xia, M. Sawan, Photoacoustic imaging for monitoring of stroke diseases: A review, Photoacoustics 23 (2021), 100287.

[39] X.L. Deán-Ben, J. Robin, D. Nozdriukhin, R. Ni, J. Zhao, C. Glück, J. Droux, J. Sendón-Lago, Z. Chen, Q. Zhou, B. Weber, S. Wegener, A. Vidal, M. Arand, M. El Amki, D. Razansky, Deep optoacoustic localization microangiography of ischemic stroke in mice, Nat. Commun. 14 (1) (2023) 3584.

[40] R. Ni, M. Vaas, W. Ren, J. Klohs, Non-invasive detection of acute cerebral hypoxia and subsequent matrix-metalloproteinase activity in a mouse model of cerebral ischemia using multispectral-optoacoustic-tomography, Neurophotonics 5 (1) (2018), 015005.

[41] M. Vaas, R. Ni, M. Rudin, A. Kipar, J. Klohs, Extracerebral tissue damage in the intraluminal filament mouse model of middle cerebral artery occlusion, Front Neurol. 8 (2017) 85.

[42] R. Ni, A. Müller Herde, A. Haider, C. Keller, G. Louloudis, M. Vaas, R. Schibli, S. M. Ametamey, J. Klohs, L. Mu, In vivo imaging of cannabinoid type 2 receptors: functional and structural alterations in mouse model of cerebral ischemia by PET and MRI, Mol. Imaging Biol. (2021).

[43] C.G. Radu, C.J. Shu, S.M. Shelly, M.E. Phelps, O.N. Witte, Positron emission tomography with computed tomography imaging of neuroinflammation in experimental autoimmune encephalomyelitis, Proc. Natl. Acad. Sci. USA 104 (6) (2007) 1937–1942.

[44] W. Ren, H. Skulason, F. Schlegel, M. Rudin, J. Klohs, R. Ni, Automated registration of magnetic resonance imaging and optoacoustic tomography data for experimental studies, Neurophotonics 6 (2) (2019) 1–10.

[45] R. Ni, A. Villois, X.L. Dean-Ben, Z. Chen, M. Vaas, S. Stavrakis, G. Shi, A. deMello, C. Ran, D. Razansky, P. Arosio, J. Klohs, In-vitro and in-vivo characterization of CRANAD-2 for multi-spectral optoacoustic tomography and fluorescence imaging of amyloid-beta deposits in Alzheimer mice, Photoacoustics 23 (2021), 100285.

[46] Y. Hu, B. Lafci, A. Luzgin, H. Wang, J. Klohs, X.L. Dean-Ben, R. Ni, D. Razansky, W. Ren, Deep learning facilitates fully automated brain image registration of optoacoustic tomography and magnetic resonance imaging, (2021).

[47] L. Ding, X. Luis Dean-Ben, C. Lutzweiler, D. Razansky, V. Ntziachristos, Efficient non-negative constrained model-based inversion in optoacoustic tomography, Phys. Med Biol. 60 (17) (2015) 6733–6750.

[48] R.C. Team, R: A language and environment for statistical computing, (2013).

[49] G. Balasundaram, L. Ding, X. Li, A.B.E. Attia, X.L. Dean-Ben, C.J.H. Ho, P. Chandrasekharan, H.C. Tay, H.Q. Lim, C.B. Ong, R.P. Mason, D. Razansky, M. Olivo, Noninvasive anatomical and functional imaging of orthotopic glioblastoma development and therapy using multispectral optoacoustic tomography, Transl. Oncol. 11 (5) (2018) 1251–1258.

[50] C. Watson, G. Paxinos, G. Kayalioglu, C. Heise, Chapter 16 - Atlas of the Mouse Spinal Cord, in: C. Watson, G. Paxinos, G. Kayalioglu (Eds.), The Spinal Cord, Academic Press, San Diego, 2009, pp. 308–379.

[51] M. Aiello, V. Alfano, E. Salvatore, C. Cavaliere, M. Picardi, R. Della Pepa, E. Nicolai, A. Soricelli, A. Vella, M. Salvatore, M. Mascalchi, [(18)F]FDG uptake of the normal spinal cord in PET/MR imaging: comparison with PET/CT imaging, EJNMMI Res 10 (1) (2020) 91.

[52] M. Sobrado, M. Delgado, E. Fernández-Valle, L. García-García, M. Torres, J. Sánchez-Prieto, J. Vivancos, R. Manzanares, M.A. Moro, M.A. Pozo, I. Lizasoain, Longitudinal studies of ischemic penumbra by using 18F-FDG PET

and MRI techniques in permanent and transient focal cerebral ischemia in rats, NeuroImage 57 (1) (2011) 45–54.
[53] H. Yuan, J.E. Frank, Y. Hong, H. An, C. Eldeniz, J. Nie, A. Bunevicius, D. Shen, W. Lin, Spatiotemporal uptake characteristics of [18]F-2-fluoro-2-deoxy-D-glucose in a rat middle cerebral artery occlusion model, Stroke 44 (8) (2013) 2292–2299.
[54] Z. Wang, C. Mascarenhas, X. Jia, Positron emission tomography after ischemic brain injury: current challenges and future developments, Transl. Stroke Res 11 (4) (2020) 628–642.
[55] D. Buck, A. Förschler, C. Lapa, T. Schuster, P. Vollmar, T. Korn, S. Nessler, C. Stadelmann, A. Drzezga, A.K. Buck, H.J. Wester, C. Zimmer, B.J. Krause, B. Hemmer, 18F-FDG PET detects inflammatory infiltrates in spinal cord experimental autoimmune encephalomyelitis lesions, J. Nucl. Med 53 (8) (2012) 1269–1276.
[56] A. Hoehne, M.L. James, I.S. Alam, J.A. Ronald, B. Schneider, A. D'Souza, T. H. Witney, L.E. Andrews, H.C. Cropper, D. Behera, G. Gowrishankar, Z. Ding, T. Wyss-Coray, F.T. Chin, S. Biswal, S.S. Gambhir, [(18)F]FSPG-PET reveals increased cystine/glutamate antiporter (xc-) activity in a mouse model of multiple sclerosis, J. Neuroinflamm. 15 (1) (2018) 55.
[57] R. Mondal, A.T. Campoy, C. Liang, J. Mukherjee, [(18) F]FDG PET/CT studies in transgenic Hualpha-Syn (A53T) Parkinson's disease mouse model of α-synucleinopathy, Front Neurosci. 15 (2021), 676257.
[58] C.J. Shu, S. Guo, Y.J. Kim, S.M. Shelly, A. Nijagal, P. Ray, S.S. Gambhir, C. G. Radu, O.N. Witte, Visualization of a primary anti-tumor immune response by positron emission tomography, Proc. Natl. Acad. Sci. USA 102 (48) (2005) 17412–17417.
[59] E. Nair-Gill, S.M. Wiltzius, X.X. Wei, D. Cheng, M. Riedinger, C.G. Radu, O. N. Witte, PET probes for distinct metabolic pathways have different cell specificities during immune responses in mice, J. Clin. Investig. 120 (7) (2010) 2641. -2641.
[60] S. Pektor, L. Hilscher, K.C. Walzer, I. Miederer, N. Bausbacher, C. Loquai, M. Schreckenberger, U. Sahin, M. Diken, M. Miederer, In vivo imaging of the immune response upon systemic RNA cancer vaccination by FDG-PET, EJNMMI Res 8 (1) (2018) 80.
[61] Z.M. Ling, Y. Tang, Y.Q. Li, H.X. Luo, L.L. Liu, Q.Q. Tu, L.H. Zhou, Evaluation of avulsion-induced neuropathology in rat spinal cords with 18F-FDG Micro-PET/CT, PLoS One 10 (5) (2015), e0127685.
[62] R.E. von Leden, R.G. Selwyn, S. Jaiswal, C.M. Wilson, G. Khayrullina, K.R. Byrnes, 18)F-FDG-PET imaging of rat spinal cord demonstrates altered glucose uptake acutely after contusion injury, Neurosci. Lett. 621 (2016) 126–132.
[63] R.L. Greenspan, V. Suprenant, F. Atem, Visualization of distal spinal cord on F-18 FDG PET/CT, Clin. Nucl. Med 37 (2) (2012) 137–141.
[64] A. Chong, H.C. Song, B.H. Byun, S.P. Hong, J.J. Min, H.S. Bom, J.M. Ha, J.K. Lee, Changes in (18)f-fluorodeoxyglucose uptake in the spinal cord in a healthy population on serial positron emission tomography/computed tomography, Chonnam Med J. 49 (1) (2013) 38–42.
[65] B.H. Do, C. Mari, J.R. Tseng, A. Quon, J. Rosenberg, S. Biswal, Pattern of 18F-FDG uptake in the spinal cord in patients with non-central nervous system malignancy, Spine 36 (21) (2011) E1395–E1401. Philos. Pa 1976.
[66] H. Emami, P. Singh, M. MacNabb, E. Vucic, Z. Lavender, J.H. Rudd, Z.A. Fayad, J. Lehrer-Graiwer, M. Korsgren, A.L. Figueroa, J. Fredrickson, B. Rubin, U. Hoffmann, Q.A. Truong, J.K. Min, A. Baruch, K. Nasir, M. Nahrendorf, A. Tawakol, Splenic metabolic activity predicts risk of future cardiovascular events: demonstration of a cardiosplenic axis in humans, JACC Cardiovasc Imaging 8 (2) (2015) 121–130.
[67] T. Wollenweber, P. Roentgen, A. Schäfer, I. Schatka, C. Zwadlo, T. Brunkhorst, G. Berding, J. Bauersachs, F.M. Bengel, Characterizing the inflammatory tissue response to acute myocardial infarction by clinical multimodality noninvasive imaging, Circ. Cardiovasc Imaging 7 (5) (2014) 811–818.
[68] L. Ding, X.L. Dean-Ben, N.C. Burton, R.W. Sobol, V. Ntziachristos, D. Razansky, Constrained inversion and spectral unmixing in multispectral optoacoustic tomography, IEEE Trans. Med Imaging 36 (8) (2017) 1676–1685.
[69] R. Ni, Z. Chen, X.L. Deán-Ben, F.F. Voigt, D. Kirschenbaum, G. Shi, A. Villois, Q. Zhou, A. Crimi, P. Arosio, R.M. Nitsch, K.P.R. Nilsson, A. Aguzzi, F. Helmchen, J. Klohs, D. Razansky, Multiscale optical and optoacoustic imaging of amyloid-β deposits in mice, Nat. Biomed. Eng. (2022).
[70] P. Vagenknecht, A. Luzgin, M. Ono, B. Ji, M. Higuchi, D. Noain, C.A. Maschio, J. Sobek, Z. Chen, U. Konietzko, J.A. Gerez, R. Riek, D. Razansky, J. Klohs, R. M. Nitsch, X.L. Dean-Ben, R. Ni, Non-invasive imaging of tau-targeted probe uptake by whole brain multi-spectral optoacoustic tomography, Eur. J. Nucl. Med Mol. Imaging (2022).
[71] N. Straumann, B.F. Combes, X.L. Dean-Ben, R. Sternke-Hoffmann, JA. Gerez, I. Dias, Z. Chen, B. Watts, I. Rostami, K. Shi, A. Rominger, CR. Baumann, J. Luo, D. Noain, RM. Nitsch, N. Okamura, D. Razansky, R. Ni, Visualizing alpha-synuclein and iron deposition in M83 mouse model of Parkinson's disease in vivo, bioRxiv [Preprint] (2023) 2023–06, 2023.06.28.546962.
[72] X.L. Deán-Ben, V. Ntziachristos, D. Razansky, Effects of small variations of speed of sound in optoacoustic tomographic imaging, Med Phys. 41 (7) (2014), 073301.
[73] X.L. Deán-Ben, V. Ntziachristos, D. Razansky, Statistical optoacoustic image reconstruction using a-priori knowledge on the location of acoustic distortions, Appl. Phys. Lett. 98 (17) (2011), 171110.
[74] N.O. Barioni, F. Derakhshan, L. Tenorio Lopes, H. Onimaru, A. Roy, F. McDonald, E. Scheibli, M.I. Baghdadwala, N. Heidari, M. Bharadia, K. Ikeda, I. Yazawa, Y. Okada, M.B. Harris, M. Dutschmann, R.J.A. Wilson, Novel oxygen sensing mechanism in the spinal cord involved in cardiorespiratory responses to hypoxia, Sci. Adv. 8 (12) (2022) eabm1444.
[75] G. Dang, X. Chen, Y. Chen, Y. Zhao, F. Ouyang, J. Zeng, Dynamic secondary degeneration in the spinal cord and ventral root after a focal cerebral infarction among hypertensive rats, Sci. Rep. 6 (2016) 22655.
[76] Z. Liu, M. Chopp, X. Ding, Y. Cui, Y. Li, Axonal remodeling of the corticospinal tract in the spinal cord contributes to voluntary motor recovery after stroke in adult mice, Stroke 44 (7) (2013) 1951–1956.
[77] X.H. Zhu, J.M. Chen, T.W. Tu, W. Chen, S.K. Song, Simultaneous and noninvasive imaging of cerebral oxygen metabolic rate, blood flow and oxygen extraction fraction in stroke mice, Neuroimage 64 (2013) 437–447.
[78] Y. Murata, K. Sakatani, T. Hoshino, N. Fujiwara, T. Kano, S. Nakamura, Y. Katayama, Effects of cerebral ischemia on evoked cerebral blood oxygenation responses and BOLD contrast functional MRI in stroke patients, Stroke 37 (10) (2006) 2514–2520.
[79] A.P. Fan, A.A. Khalil, J.B. Fiebach, G. Zaharchuk, A. Villringer, K. Villringer, C. J. Gauthier, Elevated brain oxygen extraction fraction measured by MRI susceptibility relates to perfusion status in acute ischemic stroke, J. Cereb. Blood Flow. Metab. 40 (3) (2020) 539–551.
[80] J. Shen, R. Sood, J. Weaver, G.S. Timmins, A. Schnell, M. Miyake, J.P. Kao, G. M. Rosen, K.J. Liu, Direct visualization of mouse brain oxygen distribution by electron paramagnetic resonance imaging: application to focal cerebral ischemia, J. Cereb. Blood Flow. Metab. 29 (10) (2009) 1695–1703.
[81] M. Ramos-Vega, P. Kjellman, M.I. Todorov, T.M. Kylkilahti, B.T. Bäckström, A. Ertürk, C.D. Madsen, I. Lundgaard, Mapping of neuroinflammation-induced hypoxia in the spinal cord using optoacoustic imaging, Acta Neuropathol. Commun. 10 (1) (2022) 51.
[82] W. Wu, P. Wang, J.X. Cheng, X.M. Xu, Assessment of white matter loss using bond-selective photoacoustic imaging in a rat model of contusive spinal cord injury, J. Neurotrauma 31 (24) (2014) 1998–2002.
[83] K.P. Kubelick, S.Y. Emelianov, In vivo photoacoustic guidance of stem cell injection and delivery for regenerative spinal cord therapies, Neurophotonics 7 (3) (2020), 030501.
[84] K.P. Kubelick, S.Y. Emelianov, Prussian blue nanocubes as a multimodal contrast agent for image-guided stem cell therapy of the spinal cord, Photoacoustics 18 (2020), 100166.
[85] E.M. Donnelly, K.P. Kubelick, D.S. Dumani, S.Y. Emelianov, Photoacoustic image-guided delivery of plasmonic-nanoparticle-labeled mesenchymal stem cells to the spinal cord, Nano Lett. 18 (10) (2018) 6625–6632.
[86] K.P. Kubelick, S.Y. Emelianov, A. Trimodal, Ultrasound, photoacoustic and magnetic resonance imaging approach for longitudinal post-operative monitoring of stem cells in the spinal cord, Ultrasound Med. Biol. 46 (12) (2020) 3468–3474.
[87] C. Wood, K. Harutyunyan, D.R.T. Sampaio, M. Konopleva, R. Bouchard, Photoacoustic-based oxygen saturation assessment of murine femoral bone marrow in a preclinical model of leukemia, Photoacoustics 14 (2019) 31–36.
[88] S.M. Lewis, A. Williams, S.C. Eisenbarth, Structure and function of the immune system in the spleen, Sci. Immunol. 4 (33) (2019).
[89] R. Jin, W. Zhong, S. Liu, G. Li, CD147 as a key mediator of the spleen inflammatory response in mice after focal cerebral ischemia, J. Neuroinflamm. 16 (1) (2019) 198.
[90] C.C. Caldwell, H. Kojima, D. Lukashev, J. Armstrong, M. Farber, S.G. Apasov, M. V. Sitkovsky, Differential effects of physiologically relevant hypoxic conditions on T lymphocyte development and effector functions, J. Immunol. 167 (11) (2001) 6140–6149.
[91] C.T. Ajmo Jr, D.O.L. Vernon, L. Collier, A.A. Hall, S. Garbuzova-Davis, A. Willing, K.R. Pennypacker, The spleen contributes to stroke-induced neurodegeneration, J. Neurosci. Res. 86 (10) (2008) 2227–2234.
[92] Y. Bao, E. Kim, S. Bhosle, H. Mehta, S. Cho, A role for spleen monocytes in post-ischemic brain inflammation and injury, J. Neuroinflamm. 7 (1) (2010) 92.
[93] M. Kim, S.D. Kim, K.I. Kim, E.H. Jeon, M.G. Kim, Y.R. Lim, E. Lkhagva-Yondon, Y. Oh, K. Na, Y.C. Chung, B.K. Jin, Y.S. Song, M.S. Jeon, Dynamics of T lymphocyte between the periphery and the brain from the acute to the chronic phase following ischemic stroke in mice, Exp. Neurobiol. 30 (2) (2021) 155–169.
[94] P. Sahota, F. Vahidy, C. Nguyen, T.T. Bui, B. Yang, K. Parsha, J. Garrett, A. Bambhroliya, A. Barreto, J.C. Grotta, J. Aronowski, M.H. Rahbar, S. Savitz, Changes in spleen size in patients with acute ischemic stroke: a pilot observational study, Int J. Stroke 8 (2) (2013) 60–67.
[95] A. Nous, I. Peeters, K. Nieboer, A.M. Vanbinst, J. De Keyser, S. De Raedt, Post-stroke infections associated with spleen volume reduction: A pilot study, PLoS One 15 (5) (2020), e0232497.
[96] N.L. Chiu, B. Kaiser, Y.V. Nguyen, S. Welbourne, C. Lall, S.C. Cramer, The volume of the spleen and its correlates after acute stroke, J. Stroke Cereb. Dis. 25 (12) (2016) 2958–2961.
[97] V.A. Braga, J.F. Paton, B.H. Machado, Ischaemia-induced sympathoexcitation in spinalyzed rats, Neurosci. Lett. 415 (1) (2007) 73–76.
[98] Y. Koza, E. Bayram, M.D. Aydin, C. Atalay, M.R. Onen, C. Ozturk, S. Sipal, E. Demirci, A. Levent, Predictive role of the cervical sympathetic trunk ischemia on lower heart rates in an experimentally induced stenoocclusive carotid artery model by bilateral common carotid artery ligation, Cardiovasc Toxicol. 19 (1) (2019) 56–61.
[99] J. Long, C. He, H. Dai, X. Kang, J. Zou, S. Ye, Q. Yu, Effects of transection of cervical sympathetic trunk on cognitive function of traumatic brain injury rats, Neuropsychiatr. Dis. Treat. 15 (2019) 1121–1131.
[100] F.M. Brochu, J. Brunker, J. Joseph, M.R. Tomaszewski, S. Morscher, S. E. Bohndiek, Towards quantitative evaluation of tissue absorption coefficients using light fluence correction in optoacoustic tomography, IEEE Trans. Med Imaging 36 (1) (2017) 322–331.

[101] R.S. Rodrigues, F.A. Bozza, C.J. Hanrahan, L.M. Wang, Q. Wu, J.M. Hoffman, G. A. Zimmerman, K.A. Morton, 18)F-fluoro-2-deoxyglucose PET informs neutrophil accumulation and activation in lipopolysaccharide-induced acute lung injury, Nucl. Med Biol. 48 (2017) 52–62.
[102] M.A. Kimm, S. Tzoumas, S. Glasl, M. Omar, P. Symvoulidis, I. Olefir, E. J. Rummeny, R. Meier, V. Ntziachristos, Longitudinal imaging of T cell-based immunotherapy with multi-spectral, multi-scale optoacoustic tomography, Sci. Rep. 10 (1) (2020) 4903.
[103] B. Manwani, K. Bentivegna, S.E. Benashski, V.R. Venna, Y. Xu, A.P. Arnold, L. D. McCullough, Sex differences in ischemic stroke sensitivity are influenced by gonadal hormones, not by sex chromosome complement, J. Cereb. Blood Flow. Metab. 35 (2) (2015) 221–229.
[104] D. Alexander, C.B. Neal, N. Vasilis, Multispectral optoacoustic tomography at 64, 128, and 256 channels, J. Biomed. Opt. 19 (3) (2014) 1–11.
[105] A. Taruttis, S. Morscher, N.C. Burton, D. Razansky, V. Ntziachristos, Fast multispectral optoacoustic tomography (MSOT) for dynamic imaging of pharmacokinetics and biodistribution in multiple organs, PLOS ONE 7 (1) (2012), e30491.
[106] C.W. Kimbrough, A. Khanal, M. Zeiderman, B.R. Khanal, N.C. Burton, K. M. McMasters, S.M. Vickers, W.E. Grizzle, L.R. McNally, Targeting acidity in pancreatic adenocarcinoma: multispectral optoacoustic tomography detects pH-low insertion peptide probes (In Vivo), Clin. Cancer Res. 21 (20) (2015) 4576.
[107] E. Merčep, J.L. Herraiz, X.L. Deán-Ben, D. Razansky, Transmission–reflection optoacoustic ultrasound (TROPUS) computed tomography of small animals, Light.: Sci. Appl. 8 (1) (2019) 18.
[108] A. Denes, J.M. Pradillo, C. Drake, H. Buggey, N.J. Rothwell, S.M. Allan, Surgical manipulation compromises leukocyte mobilization responses and inflammation after experimental cerebral ischemia in mice, Front Neurosci. 7 (2013) 271.
[109] H.K. Eltzschig, P. Carmeliet, Hypoxia and inflammation, N. Engl. J. Med 364 (7) (2011) 656–665.

Dr. Ruiqing Ni obtained her BSc in Pharmacy at Fudan University, China. She completed a Ph.D. in Medicine at Karolinska Institutet, Sweden. She is currently group leader at University of Zurich. Her research focuses on the development of positron emission tomography, optical imaging and magnetic resonance imaging bio-markers for diagnosis of Alzheimer's disease.

Ms Nadja Straumann is a Master student at Biology, Neurosciences at University of Zurich.

Ms Serana Fazio is a PhD student at Department of Hematology, University and University Hospital Zurich (Prof. César Nombela-Arrieta group).

Dr. Xosé Luís Deán-Ben received the diploma in automatics and electronics engineering from the Universidade de Vigo in 2004. He received the PhD degree from the same university in 2009. Since 2010, he serves as a research fellow at the Lab for Multi-Scale Functional and Molecular Imaging at the Institute for Biological and Medical Imaging (IBMI), Helmholtz Center Munich. He is currently group leader and senior scientist at ETH Zurich. His major research interests are the development of new optoacoustic systems for preclinical and clinical applications and the elaboration of mathematical algorithms for fast and accurate imaging performance.

Mr Georgios Louloudis is PhD student at Institute of Biomedical Engineering, University of Zurich (Prof. Jan Klohs group).

Ms Claudia Keller is a nuclear medicine technologist at Institute for Pharmaceutical Sciences (Group Radiopharmaceutical Science), Dep. of Chemistry and Applied Biosc. ETH Zürich.

Prof. Daniel Razansky is Full Professor of Biomedical Imaging at the Faculty of Medicine, University of Zurich and Department of Information Technologies and Electrical Engineering, ETH Zurich. He earned PhD in Biomedical Engineering and MSc in Electrical Engineering from the Technion – Israel Institute of Technology and completed postdoctoral training in bio-optics at the Harvard Medical School. From 2007 until 2018 he was the Director of Multi-Scale Functional and Molecular Imaging Lab and Professor of Molecular Imaging Engineering at the Helmholtz Center and Technical University of Munich. Razansky's Lab pioneered a number of imaging technologies successfully commercialized worldwide, among them the multi-spectral optoacoustic tomography and hybrid optoacoustic ultrasound imaging. He has authored over 200 peer-review journal articles and holds 15 patented inventions in bio-imaging and sensing. He is a co-founding Editor of the Photoacoustics journal and serves on Editorial Boards of a number of journals published by Nature Publishing Group, Elsevier, IEEE and AAPM. He is also an elected Fellow of the OSA and SPIE.

Prof. Simon Ametamey is a senior scientist at the Institute for Pharmaceutical Sciences of ETH Zurich (Group Radiopharmaceutical Sciences) since April 2005. In 2006 he was appointed Titularprofessor. He earned his doctorate degree in Organic Chemistry from the University of Zurich under the guidance of with Prof. H.H. Heimgartner. Subsequently, he spent one year as a postdoctoral fellow with Prof. K. Bernhard at Hoffmann La Roche, Basel, Switzerland. In 1991, he joined the Center for Radiopharmaceutical Sciences of ETH, PSI and USZ in Villigen, Switzerland. In 1994, Simon M. Ametamey worked as a research scientist in Karolinska Institute, Stockholm, Sweden under the supervision of Prof. Christer Halldin and contributed to the synthesis of dopamine transporter PET ligands. In January 1995, Simon M. Ametamey became the group leader of the Radiotracer Synthesis research group at the Center for Radiopharmaceutical Sciences of ETH, PSI and USZ in Villigen. In 2001, he completed his habilitation in Radiopharmaceutical Chemistry at ETH Zurich, Switzerland. His research activities concentrate on the development of radiolabelled biomolecules for diagnostic application in brain diseases and tumor imaging. Currently, his research work concentrates on the development of PET ligands for glutamatergic neurotransmission and folate receptors.

Linjing Mu received her PhD in Chemistry from Nankai University, China in 1996. She worked as a postdoctoral fellow at the University of Basel and Center for Radiopharmaceutical Sciences (CRS) in Switzerland. She was appointed team leader for PET chemistry at CRS in 2004 and Research Head of Radiopharmacy since 2010. She is a senior scientist and group leader at ETH Zurich. Her research interests focus on CNS PET tracer development and the development of new ^{18}F-radiolabelling methods as well as the translation of new PET tracers into the clinic.

Prof. César Nombela-Arrieta is Associate Professor at Department of Medical Oncology and Hematology of the University and University Hospital Zurich. He graduated in Pharmacy and obtained a PhD in Immuology from the University Complutense in Madrid. He performed his postdoctoral work in the Division of Transfusion Medicine of the Children's Hospital and the Harvard Stem Cell Institute in Boston. His laboratory is focused in understanding how stromal cells of the bone marrow microenvironment regulate healthy and malignant hematopoiesis, as well as immune cell trafficking and activation in marrow tissues. The ultimate goal is to find new ways in which dysfunctional stromal-hematopoietic crosstalk maybe targeted in hematologic malignancies.

Prof. Jan Klohs obtained a BSc degree in Chemistry at the University of Wales, Swansea, United Kingdom. He completed a MSc and Ph.D. in Medical Neurosciences at the Charité University Medicine Berlin, Germany. He is currently an assistant professor for preclinical imaging at the University of Zurich. His research focuses on the development of optical imaging and magnetic resonance imaging techniques, and investigations of preclinical models of brain disease.